Technique and Application for Quantifying Dynamic Shoulder Joint Kinematics and Glenohumeral Joint Contact Patterns

by

Daniel Frank Massimini

B.S. Mechanical Engineering, University of California at Los Angeles, 2005
S.M. Mechanical Engineering, Massachusetts Institute of Technology, 2009

Submitted to the Department of Mechanical Engineering in partial fulfillment of the requirements for the degree of

Doctor of Philosophy in Mechanical Engineering

at the

MASSACHUSETTS INSTITUTE OF TECHNOLOGY

February 2014

Signature of Author ....
Department of Mechanical Engineering
December 20, 2013

Certified by ....
Guoan Li, PhD
Professor of Orthopaedic Surgery
Harvard Medical School
Thesis Supervisor

Accepted by ....
David E. Hardt, PhD
Professor of Mechanical Engineering
Massachusetts Institute of Technology
Chairman, Department for Graduate Students

Technique and Application for Quantifying Dynamic Shoulder Joint Kinematics and Glenohumeral Joint Contact Patterns

by

Daniel Frank Massimini

Submitted to the Department of Mechanical Engineering on December 20, 2013 in partial fulfillment of the requirements for the Degree of Doctor of Philosophy in Mechanical Engineering

Abstract

The shoulder (glenohumeral) joint has the greatest range of motion of all human joints; as a result, it is particularly vulnerable to dislocation and injury. The ability to accurately measure dynamic in-vivo joint kinematics in 6-Degrees-of-Freedom (6-DOF) (translations and rotations) and subsequently quantify articular cartilage contact patterns of that joint has been and remains a difficult biomechanics problem. As a result, little is known about normal in-vivo glenohumeral joint contact patterns or the consequences of surgery on: shoulder joint kinematics, the soft tissue anatomy around the shoulder, and glenohumeral joint contact patterns. Additionally, the effect of quantifying glenohumeral joint contact patterns by means of proximity mapping, both with and without cartilage data is unknown. Therefore, the objectives of this thesis are to (1) describe and validate a non-invasive Dual Fluoroscopic Imaging System (DFIS) to measure dynamic shoulder joint motion; (2) describe a technique to quantify in-vivo glenohumeral joint contact patterns from the measured shoulder motion; (3) quantify normal glenohumeral joint contact patterns in the young healthy adult; (4) compare glenohumeral joint contact patterns determined both with and without articular cartilage data; and (5) demonstrate that the DFIS technique can evaluate the dynamic suprascapular nerve (a soft tissue around the shoulder) anatomy in 6-DOF in a proof of concept cadaveric model. Our results show that for the shoulder motion tested, glenohumeral joint contact was located on the anterior-inferior glenoid surface, and that the inclusion of articular cartilage data when quantifying in-vivo glenohumeral joint contact patterns has significant effects on the contact centroid location, the contact centroid range of travel, and the total contact path length. As a result, our technique offers an advantage over glenohumeral joint contact pattern measurement techniques that neglect articular cartilage data. Likewise, this technique may be more sensitive than traditional 6-DOF joint kinematics for the assessment of overall glenohumeral joint health. Lastly, in the proof of concept cadaveric model, we demonstrated that the DFIS technique can evaluate the dynamic suprascapular nerve anatomy in 6-DOF and that the anatomical course of the nerve may be altered by a rotator cuff tendon tear and subsequent to surgical intervention.

Guoan Li, PhD - Thesis Supervisor
Professor of Orthopaedic Surgery, Harvard Medical School

Peter T.C. So, PhD - Committee Chair
Professor of Mechanical and Biological Engineering, MIT

Alan J. Grodzinsky, PhD - Committee Member
Professor of Electrical, Mechanical, and Biological Engineering, MIT

Jon JP Warner, MD - Clinical Advisor
Professor of Orthopaedic Surgery, Harvard Medical School

Acknowledgements

I can do all things through Christ who strengthens me. Philippians 4:13

Table of Contents

List of Figures

List of Tables

Chapter 1: Introduction to Thesis

1.1 The Shoulder Joint Complex and Problem

The shoulder (glenohumeral) joint complex has the greatest range of motion of all human joints; as a result, it is particularly vulnerable to dislocation and injury. It is comprised of four linked joint articulations: the acromioclavicular, the sternoclavicular, the scapulothoracic, and the glenohumeral. The two principal joints that contribute to the shoulder's great overall range of motion and provide the bulk of stability to the shoulder joint complex are the scapulothoracic and glenohumeral joints. The scapulothoracic joint is the tethering of the scapula to the thoracic rib cage by the subscapularis muscle, the serratus anterior muscle and the interdigitated fascia. Scapulothoracic motion is a product of the gliding articulation and force transmission of the scapula onto the thoracic rib cage through the subscapularis and serratus anterior muscles sandwiched between the bony surfaces. Conversely, the glenohumeral joint motion is derived by diarthrosis: a joint interaction through opposing articular cartilage layers. Glenohumeral joint motion is a result of a constant-contact/force transmission between the humeral head cartilage on the humerus and the glenoid cartilage on the scapula. Osteoarthritis (OA) is the progressive degenerative breakdown of articular cartilage within a diarthodial joint that causes painful bone-on-bone contact which can severely limit the range of motion of the affected joint. This significantly diminishes an individual's quality of life. OA of the shoulder typically begins during the 6th decade of life. Treatment for end stage glenohumeral OA is total shoulder arthroplasty. However, OA can occur in younger individuals after injury and subsequent to surgical intervention. One hypothesis is that glenohumeral joint contact patterns are altered in the injured/surgically augmented state, and that altered contact patterns serve to initiate and progress OA in-vivo. However, the ability to accurately measure articular cartilage contact patterns of all human joints has been and remains a difficult biomechanics problem. For that reason, little is known about normal in-vivo glenohumeral joint contact patterns or the consequences that injury and/or surgery have on altering these patterns. It is therefore essential to have a tool to accurately quantify in-vivo articular cartilage contact patterns, so that one day we can answer these questions; one method is presented in this thesis.

1.2 *Overview and Objectives*

The objectives of this thesis are to (1) describe and validate a non-invasive Dual Fluoroscopic Imaging System (DFIS) to measure dynamic shoulder joint motion; (2) describe a technique to quantify in-vivo glenohumeral joint contact patterns from the measured shoulder motion; (3) quantify normal glenohumeral joint contact patterns in the young healthy adult during scapular plane abduction adduction motion with external humeral rotation; (4) compare glenohumeral joint contact patterns determined both with and without articular cartilage data; and (5) demonstrate that the DFIS technique can evaluate the dynamic suprascapular nerve (a soft tissue around the shoulder) anatomy in 6-DOF in a proof of concept cadaveric model and show that the anatomical course of the nerve may be altered by a rotator cuff tendon tear and subsequent to surgical intervention.

The format of this thesis is a composition of three manuscripts, making for three main chapters: 2, 3, and 4. The manuscripts of chapters 2 and 4 have been previously published through the peer-review process. The text and figures contained in both chapters 2 and 4 are directly copied from their respective published journal articles and formatted for the MIT thesis guidelines. As an author of these articles, the publisher (Elsevier) grants me (an author) an unrestricted license to reuse my previous published work in my (the author's) thesis. Chapter 3 will be submitted for journal publication simultaneously with submission of this thesis. In chapter 2, I will describe and validate a non-invasive marker-less tracking technique for measuring dynamic shoulder joint kinematics by way of a Dual Fluoroscopic Imaging System (DFIS), satisfying objective (1). In chapter 3, I will describe a technique to quantify in-vivo glenohumeral joint contact patterns, satisfying objective (2). Additionally, in chapter 3, I will quantify normal glenohumeral joint contact patterns in the young healthy adult and compare these contact patterns that were determined with and without articular cartilage data, satisfying objectives (3) and (4). In chapter 4, I will apply the validated bone model tracking technique for measuring dynamic shoulder joint kinematics described in chapter 2, to a clinical relevant shoulder joint injury (rotator cuff tendon tear) and surgical intervention model. In the process, I will describe a novel method for tracking nerves (soft tissue) in three dimensions (6-DOF) during dynamic simulated shoulder joint motion in a cadaveric proof of concept model, satisfying objective (5).

1.3 Related Publications

1. Boyer, P. J.; **Massimini, D. F.**; Gill, T. J.; Papannagari, R.; Stewart, S. L.; Warner, J. P.; and Li, G.: In vivo articular cartilage contact at the glenohumeral joint: preliminary report. *J Orthop Sci,* 13(4): 359-65, 2008.

2. Elhassan, B.; Ozbaydar, M.; Diller, D.; **Massimini, D.**; Higgins, L. D.; and Warner, J. J.: Open versus arthroscopic acromioclavicular joint resection: a retrospective comparison study. *Arthroscopy,* 25(11): 1224-32, 2009.

3. Elhassan, B.; Ozbaydar, M.; **Massimini, D.**; Diller, D.; Higgins, L.; and Warner, J. J.: Transfer of pectoralis major for the treatment of irreparable tears of subscapularis: does it work? *J Bone Joint Surg Br,* 90(8): 1059-65, 2008.

4. Elhassan, B.; Ozbaydar, M.; **Massimini, D.**; Higgins, L.; and Warner, J. J.: Arthroscopic capsular release for refractory shoulder stiffness: a critical analysis of effectiveness in specific etiologies. *J Shoulder Elbow Surg,* 19(4): 580-7, 2010.

5. **Massimini, D. F.**; Boyer, P. J.; Papannagari, R.; Gill, T. J.; Warner, J. P.; and Li, G.: In-vivo glenohumeral translation and ligament elongation during abduction and abduction with internal and external rotation. *J Orthop Surg Res,* 7: 29, 2012.

6. **Massimini, D. F.**; Li, G.; and Warner, J. P.: Glenohumeral contact kinematics in patients after total shoulder arthroplasty. *J Bone Joint Surg Am,* 92(4): 916-26, 2010.

7. **Massimini, D. F.**; Singh, A.; Wells, J. H.; Li, G.; and Warner, J. J.: Suprascapular nerve anatomy during shoulder motion: a cadaveric proof of concept study with implications for neurogenic shoulder pain. *J Shoulder Elbow Surg*, 2012.

8. **Massimini, D. F.**; Warner, J. J.; and Li, G.: Non-invasive determination of coupled motion of the scapula and humerus-An in-vitro validation. *J Biomech,* 44(3): 408-12, 2011.

9. Ozbaydar, M.; Elhassan, B.; Diller, D.; **Massimini, D.**; Higgins, L. D.; and Warner, J. J.: Results of arthroscopic capsulolabral repair: Bankart lesion versus anterior labroligamentous periosteal sleeve avulsion lesion. *Arthroscopy,* 24(11): 1277-83, 2008.

10. Zhu, Z.; **Massimini, D. F.**; Wang, G.; Warner, J. J.; and Li, G.: The accuracy and repeatability of an automatic 2D-3D fluoroscopic image-model registration technique for determining shoulder joint kinematics. *Med Eng Phys*, 2012.

For completeness, I am currently preparing three manuscripts for journal publication.

Chapter 2: Technique and Validation

2.1 *Preface*

In chapter 2, I describe a non-invasive marker-less tracking technique for measuring dynamic shoulder joint kinematics by way of a Dual Fluoroscopic Imaging System (DFIS). The technique was validated in a cadaveric model, and the accuracy determined by comparison to a marker-based gold standard. The technique described in this chapter serves as the framework that subsequent analysis can be layered upon. One example would be the determination of glenohumeral joint contact patterns by means of proximity mapping from known shoulder joint kinematics, which I will describe in chapter 3.

The text and figures contained in chapter 2 are directly copied from the Elsevier published journal article shown in the journal header below and formatted for the MIT thesis guidelines. As an author of this article, Elsevier grants me (an author) an unrestricted license to reuse my previous published work in my (the author's) thesis. No transfer of copyright is required between the authors, Elsevier and the Massachusetts Institute of Technology.

Journal of Biomechanics 44 (2011) 408–412

ELSEVIER

Contents lists available at ScienceDirect

Journal of Biomechanics

journal homepage: www.elsevier.com/locate/jbiomech
www.JBiomech.com

Non-invasive determination of coupled motion of the scapula and humerus—An in-vitro validation

Daniel F. Massimini [a,b], Jon J.P. Warner [a], Guoan Li [a,*]

[a] Massachusetts General Hospital, Harvard Medical School, Bioengineering Laboratory, GRJ-1215, 55 Fruit Street, Boston, MA 02114, USA
[b] Massachusetts Institute of Technology, Department of Mechanical Engineering, 77 Mass Ave, Cambridge, MA 02139, USA

A R T I C L E I N F O

Article history:
Accepted 7 October 2010

2.2 *Abstract*

Measuring the motion of the scapula and humerus with sub-millimeter levels of accuracy in six-degrees-of-freedom (6-DOF) is a challenging problem. The current methods to measure shoulder joint motion via the skin do not produce clinically significant levels of accuracy. Thus, the purpose of this study was to validate a non-invasive markerless dual fluoroscopic imaging system (DFIS) model-based tracking technique for measuring dynamic in-vivo shoulder kinematics. Our DFIS tracks the positions of bones based on their projected silhouettes to contours on recorded pairs of fluoroscopic images. For this study, we compared markerlessly tracking the bones of the scapula and humerus to tracking them with implanted titanium spheres using a radiostereometric analysis (RSA) while manually manipulating a cadaver specimen's arms. Additionally, we report the repeatability of the DFIS to track the scapula and humerus during dynamic shoulder motion. The difference between the markerless model-based tracking technique and the RSA was ±0.3mm in translation and ±0.5° in rotation. Furthermore, the repeatability of the markerless DFIS model-based tracking technique for the scapula and humerus was ±0.2mm and ±0.4°, respectively. The model-based tracking technique achieves an accuracy that is similar to an invasive RSA tracking technique and is highly suited for non-invasively studying the in-vivo motion of the shoulder. This technique could be used to investigate the scapular and humeral biomechanics in both healthy individuals and in patients with various pathologies under a variety of dynamic shoulder motions encountered during the activities of daily living.

2.3 Introduction

The shoulder joint, often referred to as the glenohumeral joint in most biomechanical studies, has the greatest range-of-motion of any joint in the human body. An in-depth understanding of shoulder joint biomechanics is instrumental for helping prevent shoulder injury and improving surgical treatment modalities for shoulder pathologies. However, due to its complicated anatomy and large range-of-motion, measuring the dynamic in-vivo kinematics of the shoulder joint is a challenging problem in the field of biomechanics.

Numerous techniques have been developed to study the in-vivo biomechanics of the human shoulder. A comprehensive review of techniques has been compiled by Hill et al.[22] In a brief summary, in-vivo dynamic shoulder biomechanics have been investigated using the following modalities: electromagnetic tracking,[6,8,12,13,31] single plane fluoroscopy,[27,33] magnetic resonance imaging,[16,17,23,34,39] radiostereometric analysis (RSA),[10,20,21] biplane radiography,[2-4] and optical motion tracking.[1,11,14,24,32] Additionally, a dual plane fluoroscopic imaging system (DFIS)[29] has been used to report glenohumeral contact kinematics in healthy volunteers[7] and in patients with total shoulder arthroplasty[30] during quasi-static shoulder motion. However, the use of a DFIS for tracking the scapula and humerus during dynamic shoulder motion has not been assessed.

Therefore, the purpose of this study was to validate a non-invasive markerless model-based tracking technique using a DFIS to quantify the kinematics of the scapula and humerus during dynamic shoulder motion. A radiostereometric analysis (RSA)[10,26,37,40] marker-based tracking technique was used as a reference for measuring shoulder kinematics during simulated shoulder motion of a cadaver specimen. Previously our laboratory has validated this technique in the knee,[28] spine,[42] and ankle;[41] and based upon these results, we hypothesized that the technique would track the scapula and humerus similarly to the RSA. In addition, the repeatability of the DFIS model-based tracking was assessed for the scapula and humerus in 6-DOF.

2.4 *Materials and Methods*

Specimen Preparation

One male fresh-frozen cadaver torso (age 30) with upper extremities intact was acquired. The specimen was stored at -20°C until thawed at room temperature for testing. Titanium spheres 1/8" diameter were implanted into the scapula and humerus of both shoulders by an orthopaedic surgeon. For the scapula, a superior approach was utilized along the scapular spine. One sphere was implanted into the acromion, three spheres along the scapular spine and one sphere near the spinoglenoid notch. For the humerus, a deltopectoral approach was utilized to directly visualize the lateral aspect of the humeral head. Five spheres were implanted broadly distributed into the lateral cortical bone of the humeral head and away from the articular cartilage. The procedure used to implant the titanium sphere was to (1) directly visualize the location to implant the sphere; (2) mark the location with the tip of a Steinman pin; (3) drill a 3/32" diameter hole through the marked location; and (4) gently hammer the sphere into the undersized hole until flush with the bone surface. The compression of the cortical bone securely held the spheres from dislodging. A running locking stitch was used to close the deltopectoral and superior approaches.

Bone Model Reconstruction

The specimen was CT scanned in a LightSpeed Pro 16 (GE Healthcare). The scanner captured the torso in 281 axial slices with an image spacing of 0.625mm, capturing from the acromion to approximately the mid-shaft of the humerus. The field of view was approximately 280 by 420mm with an image resolution of 512 by 512 pixels. DICOM files of the scan were transferred to a personal computer and automatically segmented by an in-house custom MATLAB (The Mathworks Inc, Natick, MA) script based on the intensity gradient of each pixel. The segmented contours were imported into Rhinoceros 3D (Robert McNeel & Associates, Seattle, WA) and arranged into layers that corresponded to the CT slice spacing of 0.625mm. B-splines were connected between the segmented contours to create 3D surface meshes of the scapula and humerus (Figure 1). The average mesh size was 30,000 polygons and 15,000 vertices. Two sets of bone models were reconstructed, one with titanium spheres for RSA tracking and one with the spheres removed for model-based tracking.

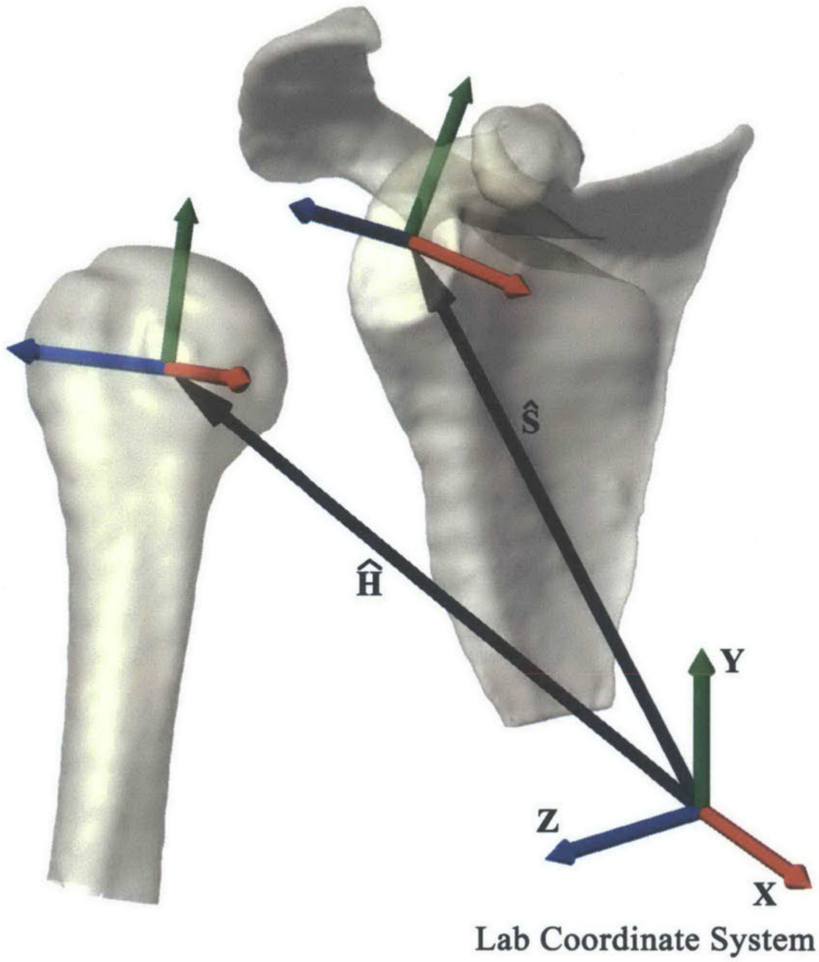

Figure 1 Reconstructed scapula and humerus bone models with coordinate systems. The vector $\hat{S}$ is the position of the scapula to the fixed global coordinate system. Similarly, the vector $\hat{H}$ is the position of the humerus to the fixed laboratory coordinate system.

On the right shoulder complex, a coordinate system was created on the scapula by constructing a line between the superior and inferior rim of the glenoid. The midpoint of this line was taken as the origin. The positive Y-axis was defined along this line in the direction of the origin to the superior rim. The positive X-axis was defined perpendicular to the Y-axis in the direction of the origin to the anterior glenoid rim. The positive Z-axis was constructed as the cross product of the X-axis into the Y-axis (Figure 1). Similarly, a humeral coordinate system was created by fitting a sphere to the humeral head. The center of the sphere was taken as the origin. The Y-axis was defined along the line from an area centroid of the bony contour of the humeral shaft (from an axial slice approximately 10cm distal to the origin) to the origin. The positive sense of the Y-axis was from the origin in the direction of distal to proximal. The positive Z-axis was defined perpendicular to the Y-axis from the origin in the direction of the greater tuberosity. Lastly, the positive X-axis was constructed as the cross product of the Y-axis and the Z-axis (Figure 1). A coordinate system for the left shoulder complex was created similar to the right shoulder complex, but the direction of the Z-axis was flipped to maintain a right hand coordinate system.

Testing Procedure

Immediately following the CT scan, the specimen was rigidly fixed with eight 3" drywall screws to a 1.25" acrylic plate as part of a custom apparatus through the pedicles of the spine (Figure 2). The experimental setup allowed for unconstrained motion of both shoulders while not permitting lateral bending, flexion/extension and twist of the trunk. The shoulder tested was placed with the glenohumeral joint centered in the imaging volume created by the dual fluoroscopes. Details of the imaging system[29] have been previously described. Briefly however, the system consists of two digital fluoroscopes (12" BV Pulsera, Phillips Medical, USA) arranged with the image intensifiers skewed from the orthogonal at approximately 120° to permit unconstrained motion of the shoulder joint. The typical fluoroscope settings were 55kV and 0.5mA. Images were acquired with a pulse width of 8ms and 30 frames per second. These image settings deliver an equivalent ionizing radiation dose of 0.072uSv per image pair or equivalently 0.26mSv per minute for both fluoroscopes.

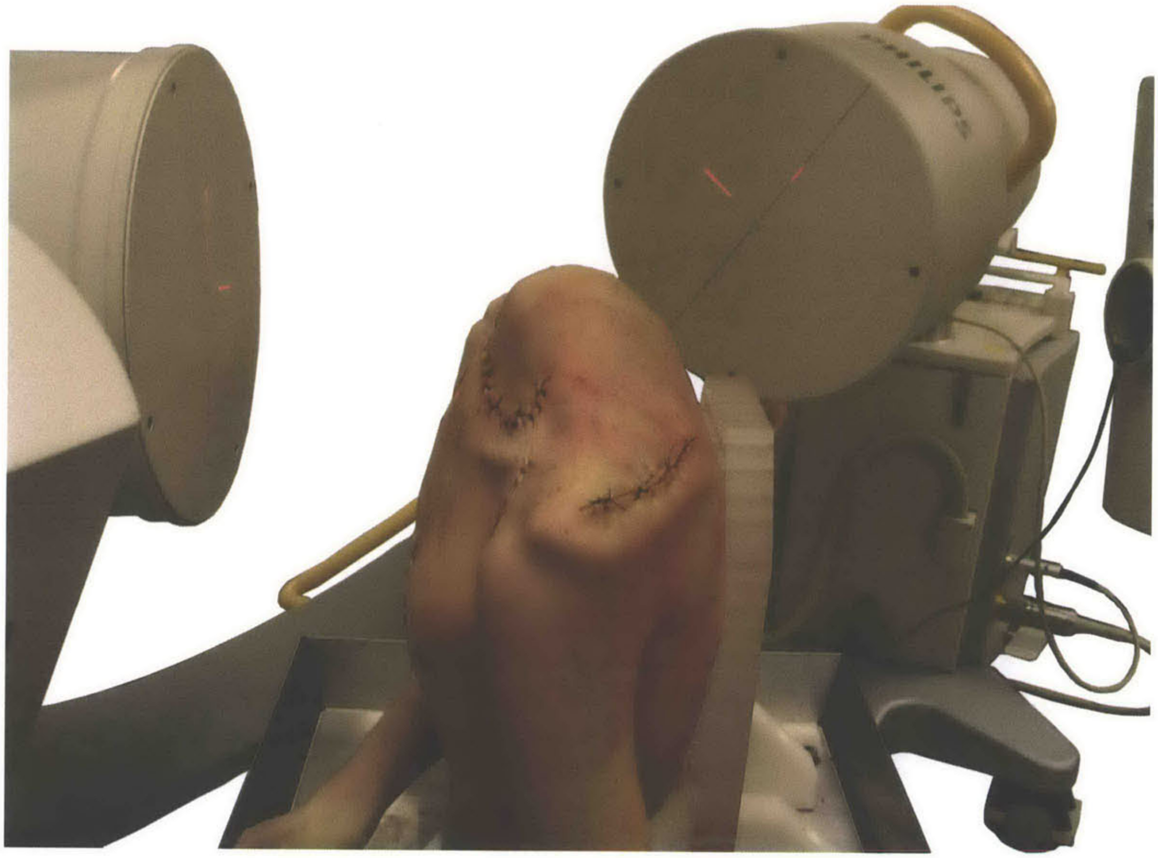

Figure 2 Dual fluoroscopic imaging system (DFIS) shown with the cadaver specimen in the custom apparatus used for testing.

Two motion patterns were simulated by manually manipulating the specimen's arms: abduction/adduction and internal/external rotation. The right shoulder was tested in abduction/adduction at approximately 79°/sec and 180°/sec and in internal/external rotation at 118°/sec. The left shoulder was tested in abduction/adduction at approximately 62°/sec and 128°/sec and in internal/external rotation at 65°/sec. Abduction/adduction motion was in the coronal plane and simulated approximately at 0°-130°-0° cycle (abduction beyond 130° was not tested as superior migration of the humeral head was noted causing impingement). Internal/external rotation of the humerus about its long axis was in the scapular plane at 90° abduction of the humerus to the vertical and simulated a cycle from maximum internal to external to internal rotation (approximately 360° total rotation). In total, six motion patterns were simulated. The rotation rates were controlled with a stopwatch. The objective was a fast and slow abduction/adduction cycle for each shoulder. For the right shoulder, 79°/sec ≈ 3sec cycle and 180°/sec ≈ 1.5sec cycle. For the left shoulder, 62°/sec ≈ 4sec cycle and 128°/sec ≈ 2sec cycle. For internal/external rotation, we arbitrarily chose which shoulder received the fast or slow rotation rate of 118°/sec ≈ 3sec cycle and 65°/sec ≈ 6sec cycle.

Dual Fluoroscopic Imaging System (DFIS)

The recorded fluoroscopic image pairs were transferred to a personal computer workstation (2.4 GHz Xeon Quad Core, Dell Inc, USA) for image processing and analysis. Each image was corrected for geometric distortion caused by environmental perturbations of the X-ray beam and from the slightly curved surface of the image intensifier. An adapted Gronenschild[18,19] global surface mapping technique was utilized. A virtual representation of the physical DFIS was created in solid modeling software (Rhinoceros 3D, Robert McNeel & Associates, Seattle, WA) to identically match the geometry of the physical fluoroscopes used for testing, termed a virtual DFIS. The corrected pairs of fluoroscopic images were imported into the virtual DFIS and placed on their respective virtual intensifier. Similarly, the reconstructed 3D bone models of the scapula and humerus were imported into the virtual DFIS for kinematics reconstruction.

Model-Based Tracking Technique

The technique of model-based tracking has its roots in stereophotogrammetry.[35] To briefly summarize this technique, a ray trace is constructed from a point on an image plane to the source location from two or more independent views. The intersection of these rays determines the 3D position of the point in space. By simultaneously tracking multiple points on an object, the 3D position of the object in space can be determined. Model-based tracking employs a variation of this technique to determine the 3D object position based on its projected silhouette to segmented contour in place of individual points. The scapula and humerus bone contours were manually segmented from the fluoroscopic images within the virtual DFIS. Bone models of the scapula and humerus with titanium spheres removed were manually translated and rotated within the virtual DFIS until their projected silhouettes aligned with the segmented contours on both image planes simultaneously; thereby recreating the positions of the scapula and humerus (Figure 3). One researcher (D.F.M) performed all data analysis. This model-based tracking procedure was independently repeated for select sequential image pairs recorded by the DFIS corresponding to approximately 30° of humeral motion between selected image pairs in this validation study.

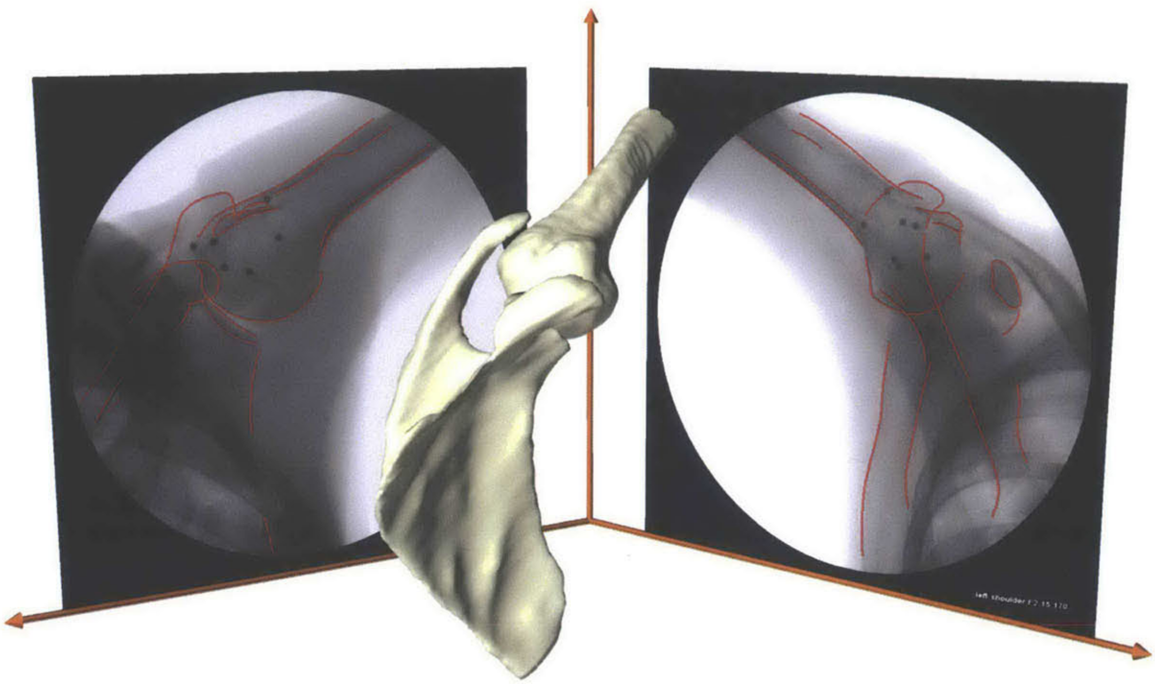

Figure 3 Virtual DFIS with reconstructed scapula and humerus bone models. The orientation of the models has been aligned to the contours recreating the position of the scapula and humerus.

RSA Marker-Based Tracking Technique

RSA is a tracking technique similarly rooted in stereophotogrammetry.[35] In summary, the technique utilizes ray trace intersections of implanted metallic spheres to determine the 3D position of objects in space. This technique was adapted to a DFIS, where the bone models of the scapula and humerus with titanium spheres were aligned with the intersection of the ray traces from the spheres on the fluoroscopic images. This marker-based tracking procedure was performed for the same sequential image pairs selected for model-based tracking.

Comparison of the Model-Based with RSA

The relative position and orientation of the scapula and humerus determined using the model-based tracking technique was compared to those determined by the RSA marker-based technique. The relative position (X, Y, and Z) was defined as the difference between the origins of the coordinate systems for the two tracking techniques. Similarly, the relative orientation was defined as the Euler angles (X-Y-Z sequence) between the coordinate systems for the two tracking techniques. The absolute values of the position and the Euler angles were used to calculate the average difference and standard deviation between the model-based and the RSA tracking techniques. This analysis method was chosen because the absolute value of the difference highlights the maximum error in translation and rotation between the two tracking techniques. Translations and rotations are reported as the [average difference ± standard deviation] in millimeters and degrees, respectively.

Model-Based Repeatability

The repeatability of the model-based tracking technique was quantified by tracking the position of the scapula and humerus with respect to a fixed laboratory coordinate system. One fluoroscopic image pair was randomly selected from each shoulder and ten independent trials of the model-based tracking procedure was performed; this included manually segmenting the fluoroscopic images each trial. A 15 minute break was taken between trials to minimize learning effects. The position and orientation of the scapula and humerus from the ten independent trials were used to calculate a standard deviation, variance and standard error of the mean in translation (X, Y, and Z) and rotation (Euler angles). The standard deviations calculated were taken as the repeatability of the model-based tracking technique. One researcher (D.F.M) extremely familiar with the matching technique performed the repeatability assessment.

2.5 *Results*

Comparison of the Model-Based with RSA

The data obtained from the dynamic non-invasive model-based tracking technique compared to the RSA marker-based technique are shown in Table 1. The average difference between the two techniques was 0.27 ± 0.19mm and 0.49 ± 0.36° for all simulated motions of the scapula and humerus. The rotation rate (62°/s, 79°/s, 128°/s, and 180°/s) of the long axis of the humerus in abduction/adduction did not influence the magnitude of the difference between the two tracking techniques. However, internal/external rotation about the long axis of the humerus from 65°/s to 118°/s showed an increase in magnitude of rotation about the long axis of the humerus from 0.78 ± 0.31° to 0.91 ± 0.35° between the two tracking techniques.

	Left Humerus				Left Scapula			
Axis	65°/s IR/ER	128°/s AB/AD	62°/s AB/AD	Average	65°/s IR/ER	128°/s AB/AD	62°/s AB/AD	Average
X (mm)	0.25 ± 0.17	0.33 ± 0.20	0.28 ± 0.19	0.29 ± 0.18	0.21 ± 0.17	0.31 ± 0.23	0.32 ± 0.19	0.28 ± 0.19
Y (mm)	0.24 ± 0.14	0.24 ± 0.19	0.34 ± 0.13	0.28 ± 0.15	0.26 ± 0.17	0.22 ± 0.13	0.32 ± 0.16	0.27 ± 0.15
Z (mm)	0.26 ± 0.20	0.36 ± 0.17	0.26 ± 0.15	0.29 ± 0.17	0.17 ± 0.10	0.22 ± 0.19	0.28 ± 0.21	0.22 ± 0.17
XX (deg)	0.63 ± 0.32	0.55 ± 0.27	0.54 ± 0.36	0.57 ± 0.31	0.38 ± 0.15	0.35 ± 0.29	0.47 ± 0.42	0.41 ± 0.30
YY (deg)	0.78 ± 0.31	0.59 ± 0.28	0.66 ± 0.26	0.68 ± 0.28	0.39 ± 0.24	0.38 ± 0.38	0.40 ± 0.21	0.39 ± 0.26
ZZ (deg)	0.31 ± 0.19	0.49 ± 0.47	0.39 ± 0.30	0.39 ± 0.32	0.39 ± 0.31	0.59 ± 0.26	0.55 ± 0.42	0.51 ± 0.34
	Right Humerus				Right Scapula			
Axis	118°/s IR/ER	180°/s AB/AD	79°/s AB/AD	Average	118°/s IR/ER	180°/s AB/AD	79°/s AB/AD	Average
X (mm)	0.22 ± 0.17	0.28 ± 0.16	0.27 ± 0.16	0.25 ± 0.16	0.31 ± 0.24	0.44 ± 0.19	0.36 ± 0.20	0.37 ± 0.21
Y (mm)	0.16 ± 0.12	0.17 ± 0.17	0.18 ± 0.16	0.17 ± 0.15	0.32 ± 0.21	0.23 ± 0.14	0.34 ± 0.23	0.30 ± 0.20
Z (mm)	0.15 ± 0.14	0.27 ± 0.22	0.15 ± 0.14	0.18 ± 0.17	0.24 ± 0.17	0.40 ± 0.39	0.35 ± 0.28	0.33 ± 0.28
XX (deg)	0.30 ± 0.25	0.63 ± 0.52	0.74 ± 0.44	0.56 ± 0.44	0.19 ± 0.14	0.24 ± 0.24	0.23 ± 0.21	0.22 ± 0.19
YY (deg)	0.91 ± 0.35	0.72 ± 0.58	0.76 ± 0.49	0.80 ± 0.47	0.43 ± 0.30	0.55 ± 0.48	0.41 ± 0.35	0.46 ± 0.37
ZZ (deg)	0.29 ± 0.23	0.57 ± 0.34	0.58 ± 0.42	0.48 ± 0.36	0.43 ± 0.34	0.31 ± 0.23	0.61 ± 0.38	0.46 ± 0.34

Table 1 Difference and standard deviation between the model-based tracking and the RSA marker based tracking technique. IR/ER refers to internal/external rotation simulated motion and AB/AD refers to abduction/adduction simulated motion.

Model-Based Repeatability

The average repeatability of the model-based tracking technique was ±0.13mm and ±0.44° for the humerus and ±0.23mm and ±0.42° for the scapula in ten independent matches for the left and right shoulder combined. The translational repeatability of the humerus was about half the magnitude of the scapula, whereas the rotational repeatability was about the same (Table 2).

Axis	Left Scapula	Right Scapula	Left Humerus	Right Humerus
X (mm)	0.31, 0.09, 0.10	0.24, 0.06, 0.08	0.12, 0.01, 0.04	0.11, 0.01, 0.04
Y (mm)	0.21, 0.05, 0.07	0.16, 0.02, 0.05	0.08, 0.01, 0.02	0.10, 0.01, 0.03
Z (mm)	0.13, 0.02, 0.04	0.31, 0.09, 0.10	0.15, 0.02, 0.05	0.20, 0.04, 0.06
XX (deg)	0.39, 0.15, 0.12	0.41, 0.17, 0.13	0.64, 0.41, 0.20	0.57, 0.33, 0.18
YY (deg)	0.37, 0.14, 0.12	0.28, 0.08, 0.09	0.43, 0.19, 0.14	0.36, 0.13, 0.11
ZZ (deg)	0.54, 0.29, 0.17	0.50, 0.25, 0.16	0.30, 0.09, 0.09	0.19, 0.04, 0.06

Table 2 Repeatability of the model-based tracking technique. Data presented as: standard deviation, variance, standard error of the mean.

2.6 *Discussion*

This study presents the translation and rotation differences between a non-invasive markerless DFIS model-based tracking technique for measuring shoulder biomechanics with respect to a widely accepted RSA[10,26,37,40] marker-based technique during simulated dynamic shoulder motion. The results show that this dynamic model-based tracking technique was close to the RSA within approximately ±0.3mm in translation and ±0.5° in rotation. The simulated shoulder motion or rotation rate did not detrimentally influence the performance of the model-based tracking technique with respect to the RSA (Table 1). Furthermore, the repeatability of the model-based tracking technique for the scapula and humerus was approximately ±0.2 mm and ±0.4°, respectively.

Our results compare favorably with current methods in RSA that have been validated[10,26,37,40] in several previous studies. However, marker-based tracking is an invasive technique[36] and puts the healthy volunteer through an unnecessary surgery. Skin mounted electromagnetic and optical tracking techniques have the ability to capture extremely fast dynamic activities, but at the expense of sub-millimeter resolution that results from skin motion artifact.[9,15,25] To overcome this limitation, percutaneous pins[31] attached directly to the bone and an electromagnetic tracking system have been used for the scapula and humerus, but this procedure is invasive and may limit the extreme motions of the shoulder by preventing skin motion over the bone. Dynamic markerless biplane radiography applied to shoulder joint kinematics has been validated by Bey et al[5] to ±0.5mm of a RSA marker-based tracking technique. The translation results we present for a non-invasive markerless DFIS tracking technique compare well with Bey et al.[5]

Therefore, the application of a non-invasive markerless DFIS model-based tracking technique in the in-vivo shoulder can quantify the 6-DOF motion of the scapula and humerus during dynamic activities. For example, the technique can be used to determine the kinematics of the healthy shoulder joint during the activities of daily living; such as reaching for the sky and scratching one's back. The model-based technique can also be used to study the pathologic shoulder from pre to post surgical intervention to help understand the role that altered kinematics have on osteoarthritis onset and progression within the shoulder.

However, it must be noted that the DFIS has certain limitations. The setup of the dual fluoroscopes can restrict some motion patterns of the shoulder joint such as throwing a baseball. In this experiment, flexion/extension was not examined as the fluoroscope setup and cadaver fixturing apparatus interfered in such a manner to restrict this motion pattern. However, for capturing the activities of daily living in healthy volunteers this will not impose a limitation, as a fixturing apparatus will not be used. In addition, fluoroscopic image acquisition using a 8ms pulse width does limit the maximum rotation[38] rate of the shoulder joint. Although in the present study, we did not determine the maximum rotation rate, but found that rotation rates up to 180°/s are within the DFIS capabilities and this was sufficient for quantifying the kinematics of the activities of daily living. Furthermore, the scapular and humeral coordinate systems were not based on the recommendations of the ISB,[43] as these require a more complete model of the humerus and scapula for anatomic landmarks. The imaging protocol employed, which images to approximately the mid-shaft of the humerus and based on a previous protocol[7] for generating 3D bone models is based on reducing living subjects' exposure to radiation and scan time. Coordinate systems based upon these 3D models does not influence the ability to investigate glenohumeral contact as has been previous studied.[7,30]

In conclusion, we present a non-invasive model-based DFIS tracking technique for quantitatively measuring the dynamic biomechanics of the human shoulder joint. This dynamic model-based tracking technique achieves an accuracy that is similar to an invasive RSA marker-based tracking technique. This technique could be a useful tool to investigate the scapular and humeral biomechanics in both healthy individuals and in patients with various pathologies under a variety of dynamic shoulder motions encountered during the activities of daily living.

2.7 *References*

1. Barrentine, S. W.; Fleisig, G. S.; Whiteside, J. A.; Escamilla, R. F.; and Andrews, J. R.: Biomechanics of windmill softball pitching with implications about injury mechanisms at the shoulder and elbow. *J Orthop Sports Phys Ther,* 28(6): 405-15, 1998.

2. Bey, M.; Kline, S.; Zauel, R.; Kolowich, P.; and Lock, T.: In Vivo Measurement of Glenohumeral Joint Contact Patterns. *EURASIP Journal on Advances in Signal Processing,* doi:10.1155/2010/162136: 6 pages, 2010.

3. Bey, M. J.; Brock, S. K.; Beierwaltes, W. N.; Zauel, R.; Kolowich, P. A.; and Lock, T. R.: In vivo measurement of subacromial space width during shoulder elevation: technique and preliminary results in patients following unilateral rotator cuff repair. *Clin Biomech (Bristol, Avon),* 22(7): 767-73, 2007.

4. Bey, M. J.; Kline, S. K.; Zauel, R.; Lock, T. R.; and Kolowich, P. A.: Measuring dynamic in-vivo glenohumeral joint kinematics: Technique and preliminary results. *J Biomech,* 41(3): 711-4, 2008.

5. Bey, M. J.; Zauel, R.; Brock, S. K.; and Tashman, S.: Validation of a new model-based tracking technique for measuring three-dimensional, in vivo glenohumeral joint kinematics. *J Biomech Eng,* 128(4): 604-9, 2006.

6. Borstad, J. D., and Ludewig, P. M.: Comparison of scapular kinematics between elevation and lowering of the arm in the scapular plane. *Clin Biomech (Bristol, Avon),* 17(9-10): 650-9, 2002.

7. Boyer, P. J.; Massimini, D. F.; Gill, T. J.; Papannagari, R.; Stewart, S. L.; Warner, J. P.; and Li, G.: In vivo articular cartilage contact at the glenohumeral joint: preliminary report. *J Orthop Sci,* 13(4): 359-65, 2008.

8. Crosbie, J.; Kilbreath, S. L.; Hollmann, L.; and York, S.: Scapulohumeral rhythm and associated spinal motion. *Clin Biomech (Bristol, Avon),* 23(2): 184-92, 2008.

9. Cutti, A. G.; Paolini, G.; Troncossi, M.; Cappello, A.; and Davalli, A.: Soft tissue artefact assessment in humeral axial rotation. *Gait Posture,* 21(3): 341-9, 2005.

10. de Bruin, P. W.; Kaptein, B. L.; Stoel, B. C.; Reiber, J. H.; Rozing, P. M.; and Valstar, E. R.: Image-based RSA: Roentgen stereophotogrammetric analysis based on 2D-3D image registration. *J Biomech,* 41(1): 155-64, 2008.

11. Dun, S.; Kingsley, D.; Fleisig, G. S.; Loftice, J.; and Andrews, J. R.: Biomechanical comparison of the fastball from wind-up and the fastball from stretch in professional baseball pitchers. *Am J Sports Med,* 36(1): 137-41, 2008.

12. Ebaugh, D. D.; McClure, P. W.; and Karduna, A. R.: Three-dimensional scapulothoracic motion during active and passive arm elevation. *Clin Biomech (Bristol, Avon),* 20(7): 700-9, 2005.

13. Fayad, F.; Roby-Brami, A.; Yazbeck, C.; Hanneton, S.; Lefevre-Colau, M. M.; Gautheron, V.; Poiraudeau, S.; and Revel, M.: Three-dimensional scapular kinematics and scapulohumeral rhythm in patients with glenohumeral osteoarthritis or frozen shoulder. *J Biomech,* 41(2): 326-32, 2008.

14. Fleisig, G. S.; Kingsley, D. S.; Loftice, J. W.; Dinnen, K. P.; Ranganathan, R.; Dun, S.; Escamilla, R. F.; and Andrews, J. R.: Kinetic comparison among the fastball, curveball, change-up, and slider in collegiate baseball pitchers. *Am J Sports Med,* 34(3): 423-30, 2006.

15. Garling, E. H.; Kaptein, B. L.; Mertens, B.; Barendregt, W.; Veeger, H. E.; Nelissen, R. G.; and Valstar, E. R.: Soft-tissue artefact assessment during step-up using fluoroscopy and skin-mounted markers. *J Biomech,* 40 Suppl 1: S18-24, 2007.

16. Graichen, H.; Stammberger, T.; Bonel, H.; Haubner, M.; Englmeier, K. H.; Reiser, M.; and Eckstein, F.: Magnetic resonance-based motion analysis of the shoulder during elevation. *Clin Orthop Relat Res,* 370: 154-63, 2000.

17. Graichen, H.; Stammberger, T.; Bonel, H.; Karl-Hans, E.; Reiser, M.; and Eckstein, F.: Glenohumeral translation during active and passive elevation of the shoulder - a 3D open-MRI study. *J Biomech,* 33(5): 609-13, 2000.

18. Gronenschild, E.: The accuracy and reproducibility of a global method to correct for geometric image distortion in the x-ray imaging chain. *Med Phys,* 24(12): 1875-88, 1997.

19. Gronenschild, E.: Correction for geometric image distortion in the x-ray imaging chain: local technique versus global technique. *Med Phys,* 26(12): 2602-16, 1999.

20. Hallstrom, E., and Karrholm, J.: Shoulder kinematics in 25 patients with impingement and 12 controls. *Clin Orthop Relat Res,* 448: 22-7, 2006.

21. Hallstrom, E., and Karrholm, J.: Shoulder rhythm in patients with impingement and in controls. *Acta Orthop,* 80(4): 456-64, 2009.

22. Hill, A. M.; Bull, A. M.; Dallalana, R. J.; Wallace, A. L.; and Johnson, G. R.: Glenohumeral motion: review of measurement techniques. *Knee Surg Sports Traumatol Arthrosc,* 15(9): 1137-43, 2007.

23. Hodge, D. K.; Beaulieu, C. F.; Thabit, G. H., 3rd; Gold, G. E.; Bergman, A. G.; Butts, R. K.; Dillingham, M. F.; and Herfkens, R. J.: Dynamic MR imaging and stress testing in glenohumeral instability: comparison with normal shoulders and clinical/surgical findings. *J Magn Reson Imaging,* 13(5): 748-56, 2001.

24. Inui, H.; Hashimoto, T.; and Nobuhara, K.: External rotation during elevation of the arm. *Acta Orthop*: 451-455, 2009.

25. Karduna, A. R.; McClure, P. W.; Michener, L. A.; and Sennett, B.: Dynamic measurements of three-dimensional scapular kinematics: a validation study. *J Biomech Eng,* 123(2): 184-90, 2001.

26. Kedgley, A. E.; Birmingham, T.; and Jenkyn, T. R.: Comparative accuracy of radiostereometric and optical tracking systems. *J Biomech,* 42(9): 1350-4, 2009.

27. Kon, Y.; Nishinaka, N.; Gamada, K.; Tsutsui, H.; and Banks, S. A.: The influence of handheld weight on the scapulohumeral rhythm. *J Shoulder Elbow Surg,* 17(6): 943-6, 2008.

28. Li, G.; Van de Velde, S. K.; and Bingham, J. T.: Validation of a non-invasive fluoroscopic imaging technique for the measurement of dynamic knee joint motion. *J Biomech,* 41(7): 1616-22, 2008.

29. Li, G.; Wuerz, T. H.; and DeFrate, L. E.: Feasibility of using orthogonal fluoroscopic images to measure in vivo joint kinematics. *J Biomech Eng,* 126(2): 314-8, 2004.

30. Massimini, D. F.; Li, G.; and Warner, J. P.: Glenohumeral contact kinematics in patients after total shoulder arthroplasty. *J Bone Joint Surg Am,* 92(4): 916-26, 2010.

31. McClure, P. W.; Michener, L. A.; Sennett, B. J.; and Karduna, A. R.: Direct 3-dimensional measurement of scapular kinematics during dynamic movements in vivo. *J Shoulder Elbow Surg,* 10(3): 269-77, 2001.

32. Murray, T. A.; Cook, T. D.; Werner, S. L.; Schlegel, T. F.; and Hawkins, R. J.: The effects of extended play on professional baseball pitchers. *Am J Sports Med,* 29(2): 137-42, 2001.

33. Nishinaka, N. et al.: Determination of in vivo glenohumeral translation using fluoroscopy and shape-matching techniques. *J Shoulder Elbow Surg,* 17(2): 319-22, 2008.

34. Rhoad, R. C.; Klimkiewicz, J. J.; Williams, G. R.; Kesmodel, S. B.; Udupa, J. K.; Kneeland, J. B.; and Iannotti, J. P.: A new in vivo technique for three-dimensional shoulder kinematics analysis. *Skeletal Radiol,* 27(2): 92-7, 1998.

35. Selvik, G.: Roentgen stereophotogrammetry. A method for the study of the kinematics of the skeletal system. *Acta Orthop Scand Suppl,* 232: 1-51, 1989.

36. Tashman, S., and Anderst, W.: In-vivo measurement of dynamic joint motion using high speed biplane radiography and CT: application to canine ACL deficiency. *J Biomech Eng,* 125(2): 238-45, 2003.

37. Valstar, E. R.; Vrooman, H. A.; Toksvig-Larsen, S.; Ryd, L.; and Nelissen, R. G.: Digital automated RSA compared to manually operated RSA. *J Biomech,* 33(12): 1593-9, 2000.

38. Varadarajan, K. M.; Moynihan, A. L.; D'Lima, D.; Colwell, C. W.; and Li, G.: In vivo contact kinematics and contact forces of the knee after total knee arthroplasty during dynamic weight-bearing activities. *J Biomech,* 41(10): 2159-68, 2008.

39. von Eisenhart-Rothe, R. M.; Jager, A.; Englmeier, K. H.; Vogl, T. J.; and Graichen, H.: Relevance of arm position and muscle activity on three-dimensional glenohumeral translation in patients with traumatic and atraumatic shoulder instability. *Am J Sports Med,* 30(4): 514-22, 2002.

40. Vrooman, H. A.; Valstar, E. R.; Brand, G. J.; Admiraal, D. R.; Rozing, P. M.; and Reiber, J. H.: Fast and accurate automated measurements in digitized stereophotogrammetric radiographs. *J Biomech,* 31(5): 491-8, 1998.

41. Wan, L.; de Asla, R. J.; Rubash, H. E.; and Li, G.: Determination of in-vivo articular cartilage contact areas of human talocrural joint under weightbearing conditions. *Osteoarthritis Cartilage,* 14(12): 1294-301, 2006.

42. Wang, S.; Passias, P.; Li, G.; and Wood, K.: Measurement of vertebral kinematics using noninvasive image matching method-validation and application. *Spine (Phila Pa 1976),* 33(11): E355-61, 2008.

43. Wu, G. et al.: ISB recommendation on definitions of joint coordinate systems of various joints for the reporting of human joint motion--Part II: shoulder, elbow, wrist and hand. *J Biomech,* 38(5): 981-992, 2005.

Chapter 3: In-vivo Glenohumeral Joint Contact

3.1 Preface

In chapter 3, I (1) describe a technique for quantifying in-vivo glenohumeral joint contact patterns during dynamic shoulder motion, (2) quantify normal glenohumeral joint contact patterns in the young healthy adult during scapular plane abduction adduction motion with external humeral rotation, and (3) compare glenohumeral joint contact patterns determined both with and without articular cartilage data. Chapter 3 is formatted as a peer-reviewed journal article and will be submitted for publication upon completion of this thesis.

The significance of this chapter is that it will present a non-invasive method to quantify in-vivo glenohumeral joint contact patterns. As a result, this technique may be more sensitive than traditional 6-DOF glenohumeral joint kinematic measurements for the assessment of overall glenohumeral joint health both in the injured joint state and after surgical intervention. Therefore, this technique will let us test the hypothesis and ask: What are normal in-vivo glenohumeral joint contact patterns, are they altered in the injured and surgically augmented state, and will these altered joint contact patterns serve to initiate and progress osteoarthritis (OA) in-vivo? Many of the premier surgical interventions for shoulder joint pathology rely on the implicit belief that glenohumeral joint contact patterns must be restored to normal in order to obtain good clinical outcomes, with a potential benefit of delaying the onset and progression of OA. However, this belief has not been tested, as prior to the method presented in this chapter, a technique did not exist to quantify in-vivo glenohumeral joint articular cartilage contact patterns. Therefore, in the future, we hope that this technique will be used to objectively quantify the effects that injury and surgical intervention have on the long-term ability to restore in-vivo glenohumeral joint contact patterns to normal. The results of these future studies will help to determine whether the restoration of glenohumeral joint contact patterns to normal are necessary to obtain good clinical outcomes and whether the restoration to normal serves to delay the onset and progression of osteoarthritis in-vivo.

3.2 *Abstract*

The shoulder (glenohumeral) joint has the greatest range of motion of all human joints; as a result, it is particularly vulnerable to dislocation and injury. The ability to non-invasively quantify in-vivo articular cartilage contact patterns of joints has been and remains a difficult biomechanics problem. As a result, little is known about normal in-vivo glenohumeral joint contact patterns or the consequences that surgery has on altering them. In addition, the effect of quantifying glenohumeral joint contact patterns by means of proximity mapping, both with and without cartilage data, is unknown. Therefore, the objectives of this study are to (1) describe a technique for quantifying in-vivo glenohumeral joint contact patterns during dynamic shoulder motion, (2) quantify normal glenohumeral joint contact patterns in the young healthy adult during scapular plane abduction adduction motion with external humeral rotation, and (3) compare glenohumeral joint contact patterns determined both with and without articular cartilage data. Our results show that the inclusion of articular cartilage data when quantifying in-vivo glenohumeral joint contact patterns has significant effects on the anterior-posterior contact centroid location, the superior-inferior contact centroid range of travel, and the total contact path length. As a result, our technique offers an advantage over glenohumeral joint contact pattern measurement techniques that neglect articular cartilage data. Likewise, this technique may be more sensitive than traditional 6-Degree-of-Freedom (6-DOF) joint kinematics for the assessment of overall glenohumeral joint health. Lastly, for the shoulder motion tested, we found that glenohumeral joint contact was located on the anterior-inferior glenoid surface.

3.3 *Introduction*

The shoulder (glenohumeral) joint has the greatest range of motion of all human joints; as a result, it is particularly vulnerable to dislocation and injury. One of the end goals of surgical intervention for the treatment of shoulder joint pathology is the implicit belief that glenohumeral joint mechanics must be restored to normal in order to obtain good clinical outcomes.[36] Specifically, the restoration of glenohumeral joint contact patterns between the articular cartilage of the humeral head and the glenoid. However, the ability to accurately measure in-vivo articular cartilage contact patterns of all human joints has been and remains a difficult biomechanics problem. Therefore, little is known about normal in-vivo glenohumeral joint contact patterns or the consequences that surgery has on altering these patterns.

Recent shoulder studies have shown that altered joint mechanics from both injury and surgical intervention lead to abnormal cartilage contact patterns, one subsequent effect being increased contact pressures.[8,10,12] Areas of cartilage that experience increased contact pressures have shown reductions in GAG (glycosaminoglycans) content through in-vivo MRI (magnetic resonance imaging) techniques such as T1rho and T2 mapping.[19,28,39] Reductions in GAG content (a measure of cartilage health) have been shown to indicate the onset and mark the progression of osteoarthritis in-vivo. Therefore, it is essential to have a tool to accurately measure articular cartilage contact patterns that can help surgeons restore normal glenohumeral joint mechanics. This restoration may help improve clinical outcomes and delay the onset and progression of arthritis.

Previous kinematic studies of the shoulder have used conventional non-invasive clinical imaging modalities, such as fluoroscopy,[20,24,31] CT (computed tomography),[1,2] and MRI.[4,11,32,33,37] Research that utilized invasive techniques to quantify glenohumeral joint contact has been performed in-vitro on cadaveric specimens.[8,10,13,23,36,38] Despite the advances in these modern shoulder motion measurement techniques, there are some limitations. For example, CT and MRI have limited dynamic imaging capabilities, as their traditional image acquisition mode was designed for static conditions. Furthermore, their relatively small imaging bore volumes significantly limit the joint motions that can be evaluated. Standard single plane fluoroscopy overcomes these imaging volume and static motion acquisitions constraints, but is not capable of accurately measuring 6-DOF (degree of freedom) shoulder kinematics.[41] Moreover, cadaveric studies are not yet fully capable of accurately simulating the in-vivo shoulder environment due to unknown muscle forces and cartilage contact pressures.

Recently, Bey and colleagues developed a combined biplane X-ray registration[7] and CT bone model-based procedure for determining dynamic in-vivo glenohumeral joint contact patterns.[5,6] The technique determines glenohumeral joint contact locations by computing a 3D minimum distance proximity map between the registered bone model positions of the humerus and scapula. One limitation of this technique is that it neglects glenohumeral articular cartilage data when determining joint contact patterns, primarily due to the difficulty of imaging cartilage on standard (non-contrast enhanced) clinical CT. The effect of including articular cartilage data when quantifying in-vivo glenohumeral joint contact patterns is currently unknown. Therefore, the objectives of this study are to (1) describe a technique for quantifying in-vivo glenohumeral joint contact patterns during dynamic shoulder motion utilizing cartilage data (obtained from non-contrast enhanced MRI), (2) quantify normal glenohumeral joint contact patterns in the young healthy adult during scapular plane abduction adduction motion with external humeral rotation, and (3) compare glenohumeral joint contact patterns determined both with and without articular cartilage data.

3.4 *Materials and Methods*

Subject Selection

After institutional review board approval and informed consent, 9 healthy right hand dominant subjects (4 males, 5 females; age 26.3 ± 2.4 years) were enrolled in the study. All subjects underwent a bilateral clinical shoulder exam to document normal range of motion and absence of scapular dyskinesis. Rotator cuff strength was measured with a handheld dynamometer and range of motion measured with a handheld gonimeter. Values reported are for the dominant (right) arm. The maximum elevation angle in forward flexion was 167 ± 11°. At 90° abduction in the coronal plane, the maximum external rotation was 96 ± 10° and the maximum internal rotation was 74 ± 13°. No gender differences in range of motion were detected. The average isolated supraspinatus force was 11.1 ± 3.0kg, external rotation force 9.3 ± 2.4kg and internal rotation force 10.5 ± 2.6kg. Male subjects were statistically stronger ($P = 0.022$) than female subjects by approximately 2.5kg in each force measurement. Subjects who did not pass the clinical exam or had pain, injury or previous surgery were excluded from study.

Dual Fluoroscopic Imaging System (DFIS)

The system consists of two production model mobile C-arm fluoroscopes (BV Pulsera, Philips Medical, USA) with 12 inch diameter image intensifiers. The mobile C-arm framework allows for a variety of DFIS configurations, facilitating motion studies of all joints in the body. The fluoroscopes are electronically synchronized to simultaneously acquire pulsed images at a hardware-limited 30Hz, with a 8ms X-ray pulse duration. Image synchronization was verified by electromagnetic radiation detectors installed at each X-ray generator. Pulsed X-ray generation helps reduce subject radiation exposure. The radiation safety committee at our institution determined that under typical testing conditions (55kV and 5.0mA) shoulder joint images are 0.144μSv per pair, or 0.26mSv per minute of simultaneous imaging. The maximum radiation dosage that any subject received was 0.52mSv.

Virtual Model Construction

Each subject, upon arrival to our institution, underwent a non-contrast 3-Tesla T2 weighted MRI (Siemens MAGNETOM Trio, A Tim System 3T, Malvern PA, USA) of both shoulders with 1.5mm axial slice spacing. Special attention was paid to ensure that the face of the glenoid was perpendicular to the axial slice direction. The viewing volume captured the entire scapula and the humerus to mid-shaft. The in-plane resolution was 0.39mm per pixel edge. The humerus and scapula bones and humeral and glenoid cartilages were manually segmented (Rhinoceros 4.0, Robert McNeal & Associates, Seattle WA, USA) from the surrounding tissue and bone. Triangular surface mesh elements were created from the segmented contours. Surface irregularities were smoothed (Geomagic Studio 12, Morrisville NC, USA) to a maximum vertex distance change of 0.39mm, with an average vertex distance change of 0.1mm preserving the shape and volume of the original segmented model. All triangular surface face elements were refined between 0.1-0.35 mm^2 per element.

Coordinate systems were established based on subject-specific anatomical landmarks. The humerus and humeral cartilage coordinate system origin was the center of a best fit sphere to the humeral cartilage mesh vertices. The positive direction of the Y-axis was defined by connecting the centroid of the humeral shaft at the level of the angulus inferior (scapula) to the origin. The X-Z plane perpendicular to the Y-axis at the origin was established. Looking down the Y-axis on the humeral head, a circle was best fit to the bicipital groove in the X-Z plane. A vector from the origin to the center of the circle was created. This vector was externally rotated 57° to define the positive Z-axis, approximately parallel to the epicondylar axis at the elbow. Previous studies[3,15,21] have shown that the relationship between the bicipital groove and the epicondylar axis is between 55.5° and 61.5° with a weighted average of 57.2° (meta-analysis[3,15,21]). The X-axis was found by the right hand rule. The humeral coordinate system formed is analogous to the axis definitions set forth by the ISB (International Society of Biomechanics). [40]

The scapula and glenoid coordinate systems were defined by determining a best fit X-Y plane through the glenoid cartilage mesh vertices. Normal to the plane in the lateral direction defined the positive Z-axis. Utilizing the axial glenoid cartilage contours, a best fit

3D line was established and projected onto the X-Y plane to divide the glenoid into superior-inferior and anterior-posterior halves. The midpoint of the projected line became the origin. The direction of the line in the superior direction defined the positive Y-axis. The X-axis was found by the right hand rule. This coordinate system is similar to the axis directions set forth by the ISB,[40] however the origin is located at the glenoid center and not at the angulus acromialis. The scapula coordinate system was located on the glenoid to facilitate the reporting of subject specific glenohumeral joint contact patterns in a physiologically relevant manner.

Testing Procedure - Recording of Subject Shoulder Motion

After MRI, subjects were posed with their right (dominant arm) shoulder in the center of the DFIS viewing volume. Pulsed simultaneous fluoroscopic images of the right shoulder were acquired at 30Hz while subjects cyclically performed abduction adduction motion in the scapular plane from 0° to approximately 110° of humerothoracic angle. To position the shoulder for testing, subjects begin with their extended arm fully adducted at their right side in neutral rotation. This was followed by flexing the elbow to 90° and then externally rotating the forearm about the humeral shaft axis to the plane of the scapula. Subjects maintained this elbow-flexed external rotation position during cyclic abduction adduction motion. Male subjects held a four pound dumbbell and female subjects a two pound dumbbell while performing one motion cycle in approximately four seconds. Subjects practiced this motion until comfortable, and then were required to rest for five minutes before image acquisition to minimize muscle fatigue. Three repetitions (approximately 12 seconds) were acquired in a continuous fashion with the middle cycle being used for analysis.

Measuring Scapula and Humerus Motion

The spatial position and alignment (6-DOF) of the scapula and humerus models were tracked from the fluoroscopic images using a semiautomatic contour-based registration technique. The technique optimizes each model's 6-DOF spatial parameters to minimize the error between the projected bone model surface and the corresponding bony contours on the fluoroscopic images. Relevant bone contours were manually segmented from the fluoroscopic images and imported into the optimization routine.[25] This semiautomatic contour based registration technique has been shown to have an accuracy of ±0.30mm and ±0.58° when tracking dynamic in-vivo shoulder motion.[41] The orientation of the humerus relative to the scapula was calculated using a YXZ Cardan sequence.[34] The YXZ Cardan angle rotation definitions described below are for the abduction adduction motion tested relative to when the scapula and humeral coordinate systems are approximately aligned, which is when the extended arm is in full adduction at the body side in neutral rotation. The first rotation (Y) quantifies motion around the humeral shaft axis (internal/external rotation). The second rotation (X) defines the elbow relative to the scapular plane (flexion/extension), and the third rotation (Z) describes the glenohumeral abduction adduction angle in the scapular plane. All reported humeral translations are relative the scapula coordinate system located on the glenoid.

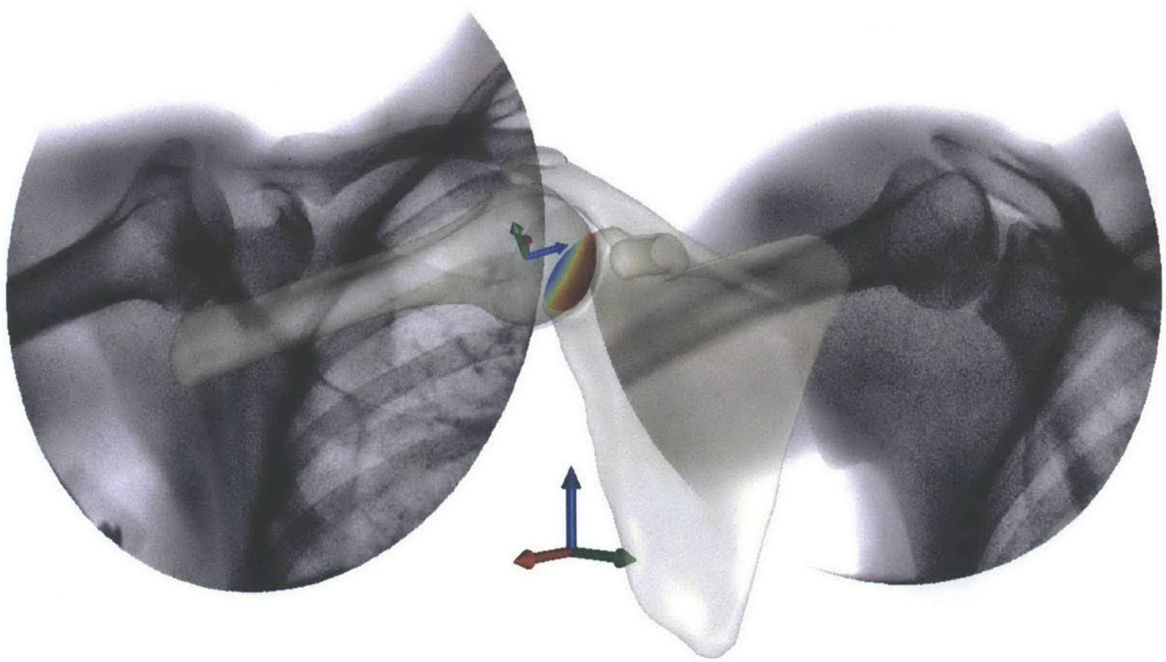

Figure 4 An illustration of the registered humerus and scapula bone models to their projections on the fluoroscopic images, taken as a snapshot in time during the dynamic shoulder motion acquired. Glenohumeral contact was superposed on the glenoid cartilage. Hot colors (red) indicate closer contact distances, whereas cool colors (blue) indicate distances that are farther away.

Quantifying Glenohumeral Joint Contact Patterns

Subject specific glenohumeral joint contact patterns were determined from the registered scapula and humerus positions for every 10% of the abduction adduction motion cycle (Figure 4). Contact patterns were calculated from: method A) humerus and scapula surface bone models, and method B) humeral cartilage and glenoid cartilage surface models. Two possibilities for surface model interactions exist: case 1) no intersection of surfaces, and case 2) intersection of surfaces. These two possibilities exist due to the absence of articular cartilage when using surface bone models alone (neglecting cartilage data), and the stacking errors resulting from the accuracy of both the DFIS model registrations and the surface model reconstructions from MRI. Custom MATLAB (The Mathworks Inc., Natick MA, USA) code was written to handle both cases automatically. For case 1, the MATLAB code determined the minimum distance from every scapula (or glenoid cartilage) surface mesh vertex to the closest location on the humerus (or humeral cartilage) surface. The contact centroid was determined by weighting the distances between 100 and 150% of the minimum distance. Shorter distances received a greater weight than longer distances. All distances greater than 150% were not used in the calculation. For case 2, the MATLAB code determined which humeral cartilage (or humerus) mesh vertices penetrated the glenoid cartilage (glenoid scapula bone) model surface. For humeral cartilage vertices that penetrated the glenoid cartilage surface, the minimum distance from each vertex to the surface was calculated. The contact centroid was determined by weighting the penetration distances between 50 and 100% of the maximum penetration distance. Longer distances received a greater weight than shorter distances. Vertices that did not penetrate the surface or distances which were less than 50% of the maximum penetration distance were not used in the calculation (Figure 5). For both cases, the centroid locations were expressed relative to the glenoid cartilage (scapula) coordinate system. To account for differences in glenoid cartilage (glenoid scapula bone) size between subjects, each subject's centroid locations were normalized to their maximum glenoid cartilage (glenoid scapula bone) dimensions in the anterior/posterior (A/P) and superior/inferior (S/I) directions. For the glenoid scapula bone measurements, the glenoid rim edge (inflection from concave to adjacent bone) was used as the measurement reference. Therefore, the contact centroid locations are expressed as a percentage of the maximum A/P (X-axis) and S/I (Y-axis) glenoid cartilage (glenoid scapula bone, rim-to-rim) dimensions.

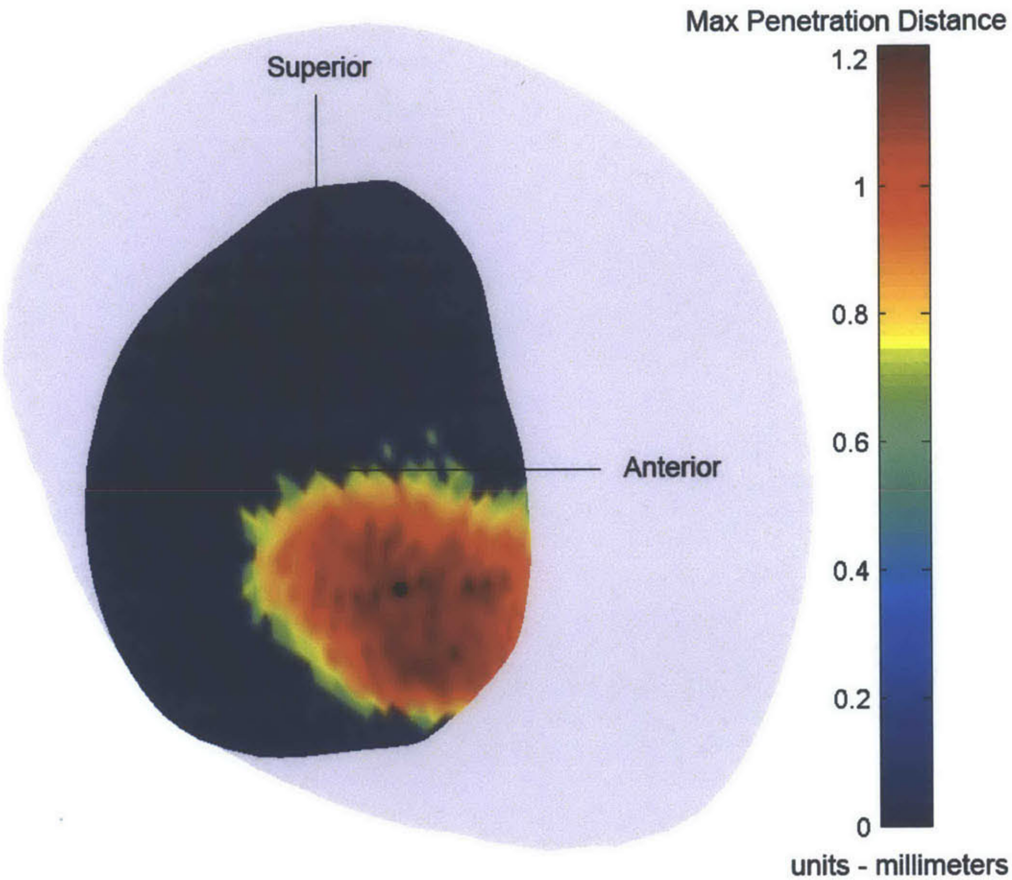

Figure 5 The MATLAB graphical proximity map output for a single subject at 20% motion cycle quantified from the cartilage surface models. The computation was a case 2 example of intersections of surfaces, where the humeral head cartilage penetrated the glenoid cartilage surface. The maximum penetration distance for this pose was 1.2mm. Weighting only the distances between 50 and 100% of the maximum gives a cutoff distance of 0.6mm. Therefore only penetration distances between 0.6 and 1.2mm were used to calculate the contact centroid location, for this specific example.

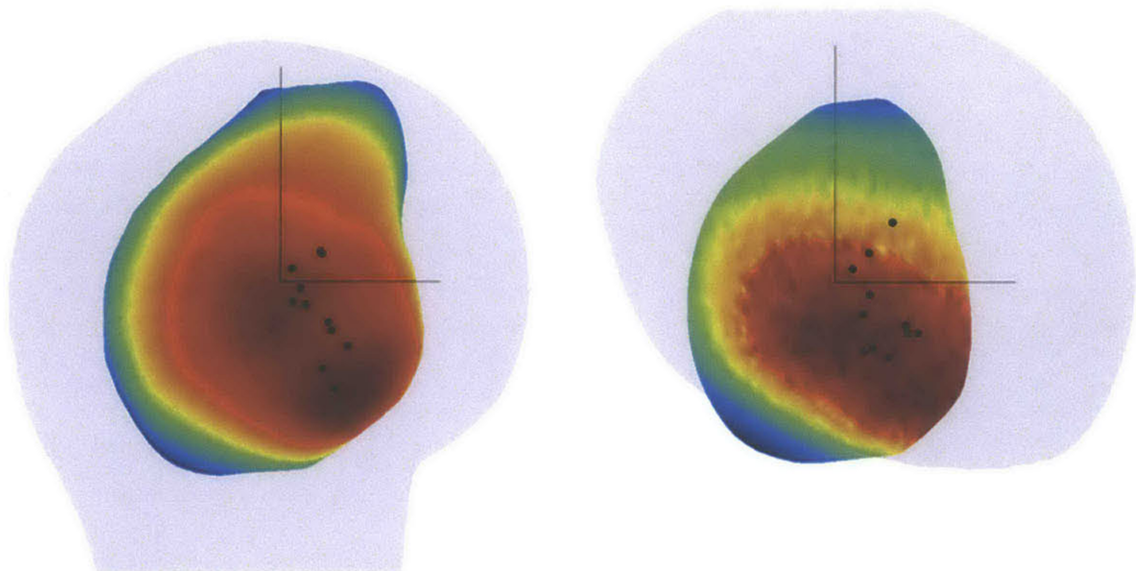

Figure 6 The MATLAB graphical output showing a single subject's glenohumeral joint contact patterns at every 10% of the motion cycle tested. Method A are the contact patterns quantified using the bone surfaces models, whereas Method B are the contact patterns quantified using the cartilage surface models. Hot colors (red) indicate closer contact distances, whereas cool colors (blue) indicate distances that are farther away. The black circles indicate the glenohumeral joint contact centroid at 10% motion cycle intervals.

Outcomes Measures and Statistical Significance

Differences in the normalized glenohumeral joint contact centroid locations calculated from: method A) humerus and scapula surface bone models, and method B) humeral cartilage and glenoid cartilage surface models (Figure 6), were quantified by five outcomes measures. All outcome measures were calculated relative to the glenoid coordinate system. These were the A/P (X-axis) and S/I (Y-axis) locations of the contact centroid, the A/P and S/I contact centroid range of travel and the total contact path length. A non-parametric Mann-Whitney U test was performed for each of the five outcome measures to determine the effect of using method A (without cartilage data) or method B (with cartilage data) for quantifying glenohumeral joint contact patterns. Statistical significance was set at $P < 0.05$. All results are presented for the right (dominant arm) shoulder and are the numerical average of all subjects for each outcome measure.

3.5 *Results*

The A/P (X-axis) glenoid cartilage width was 22.7 ± 3.4mm, whereas the A/P glenoid scapula bone width was wider at 25.8 ± 4.3mm. In the S/I (Y-axis) direction, the glenoid cartilage length (30.0 ± 3.4mm) extended to the rim-to-rim S/I glenoid scapula bone length of 30.0 ± 3.1mm. Figure 7 shows the YXZ Cardan angle relationship for the abduction adduction motion cycle tested. The maximum Cardan Z-axis glenohumeral abduction angle was 71.1 ± 14.6°. This angle was consistent with a 2-to-1 glenohumeral to scapulothoracic rhythm after the initial 30° settling phase[16] that sums to approximately 110° of the humerothoracic angle that was tested during the motion cycle. At the beginning of the motion cycle, the position of the humeral head coordinate system origin was centered A/P on the glenoid, but inferior 1.64 ± 1.29mm. Abduction from 0 to 50% (peak abduction angle) of the motion cycle translated the humerus approximately two millimeters in the anterior direction, while adduction (50 to 100% of the motion cycle) translated the humeral head posteriorly. At all times, the humeral head origin was inferior to the glenoid (X-axis) centerline (Figure 8).

The overall average (of every 10% of the motion cycle from 0 to 100%) glenohumeral joint contact centroid location was found in the anterior-inferior quadrant of the glenoid (Figure 9). The A/P (X-axis) contact centroid location from method A was anterior 12.2 ± 13.2% and from method B was anterior 15.8 ± 11.5%. There was a statistically significant difference ($P = 0.028$) in the overall average A/P contact centroid location determined from method A (without cartilage data) and from method B (with cartilage data). Conversely, we did not detect a difference in the overall average S/I contact centroid location determined from methods A and B ($P = 0.214$). Where the S/I (Y-axis) contact centroid location from method A was inferior -7.1 ± 15.1% and from method B was inferior -5.6 ± 10.8%. Figure 10 shows the glenohumeral joint contact centroid locations determined from methods A and B as a function of percent cycle motion. A/P and S/I contact centroid locations determined from method A and method B at each 10% of the motion cycle were not statistically different (Table 3).

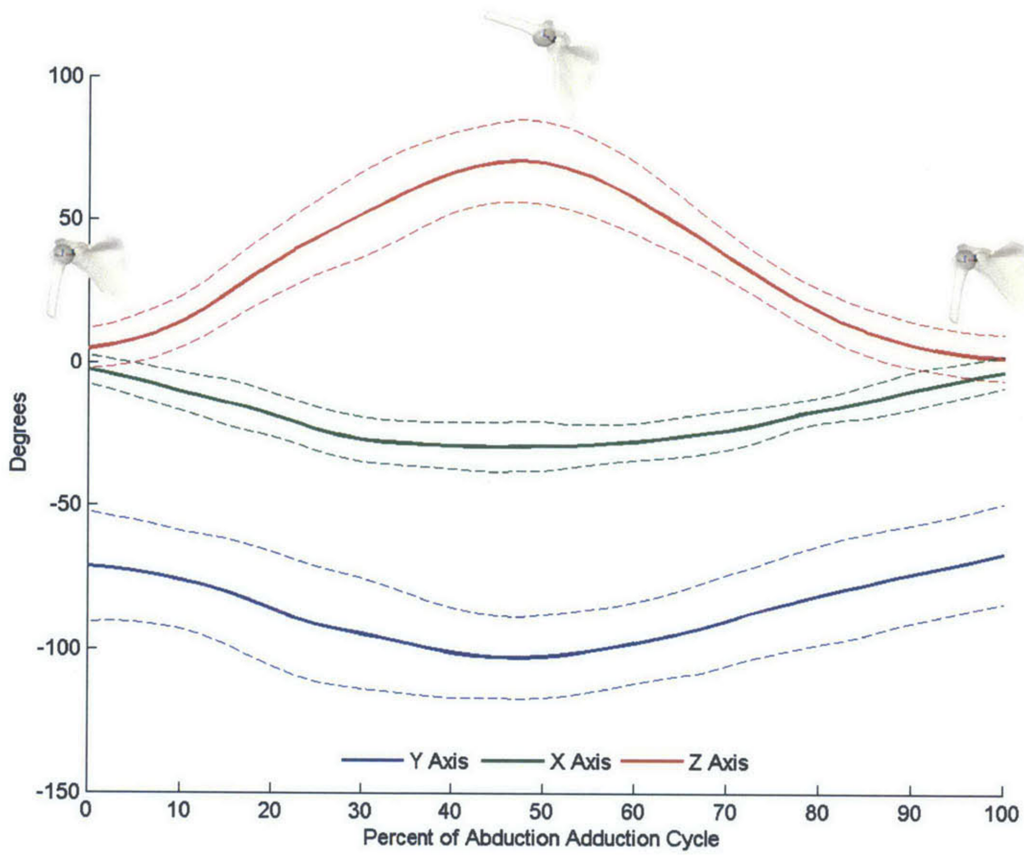

Figure 7 The average ± one standard deviation YXZ Cardan angles of all subjects for the abduction adduction motion cycle tested. The first rotation (Y-axis) quantifies motion around the humeral shaft axis (internal/external rotation). The second rotation (X-axis) defines the elbow relative to the scapular plane (flexion/extension), and the third rotation (Z-axis) describes the glenohumeral abduction adduction angle in the scapular plane.

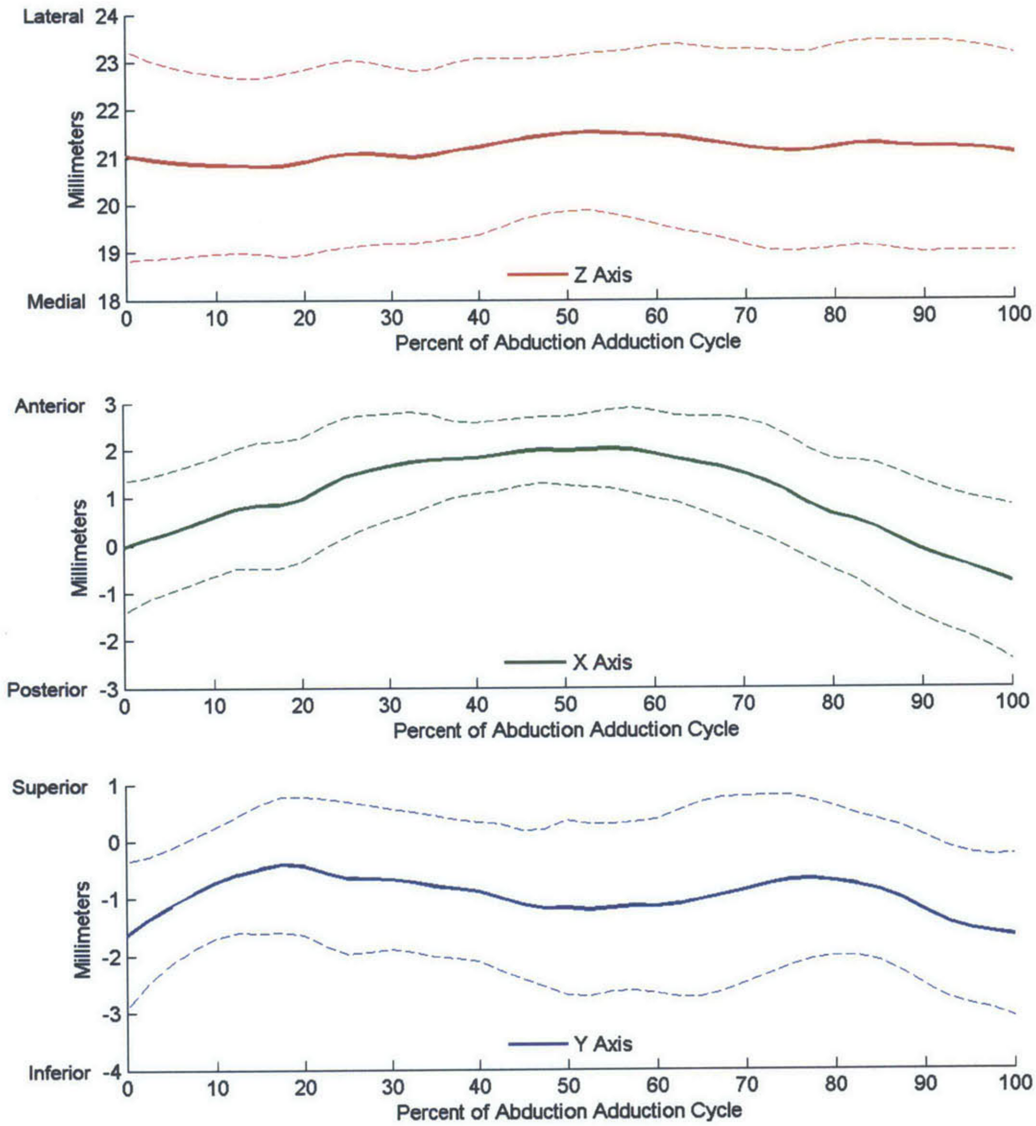

Figure 8 The average ± one standard deviation humeral head translations of all subjects for the abduction adduction motion cycle tested. The humerus translations are relative the scapula coordinate system located on the glenoid. The Z-axis results are nearly constant, which indicates that the humeral cartilage maintained contact with the glenoid cartilage for the whole motion cycle.

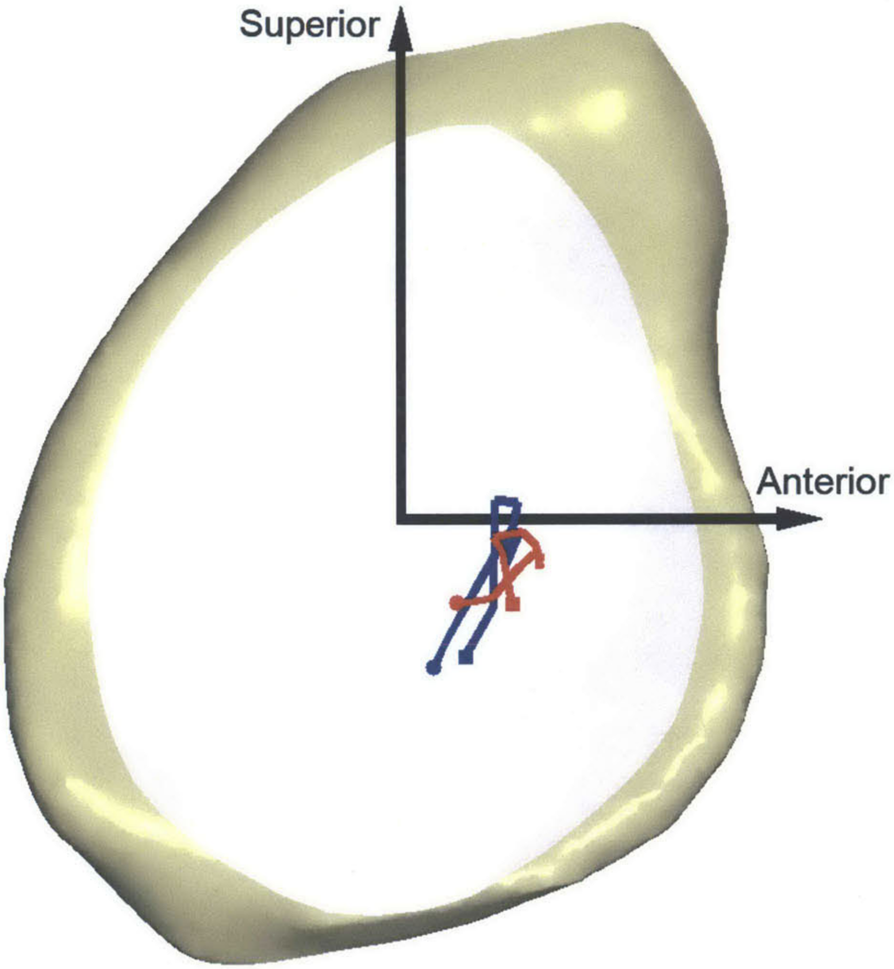

Figure 9 An illustration of the overall average (of every 10% of the motion cycle from 0 to 100%) glenohumeral joint contact path centroid locations. The blue path was determined from Method A, contact patterns quantified using the bone surfaces models, whereas the path shown in red, are the contact patterns quantified using Method B, cartilage surface models. For both methods, contact during the whole motion cycle was located on the anterior-inferior glenoid surface.

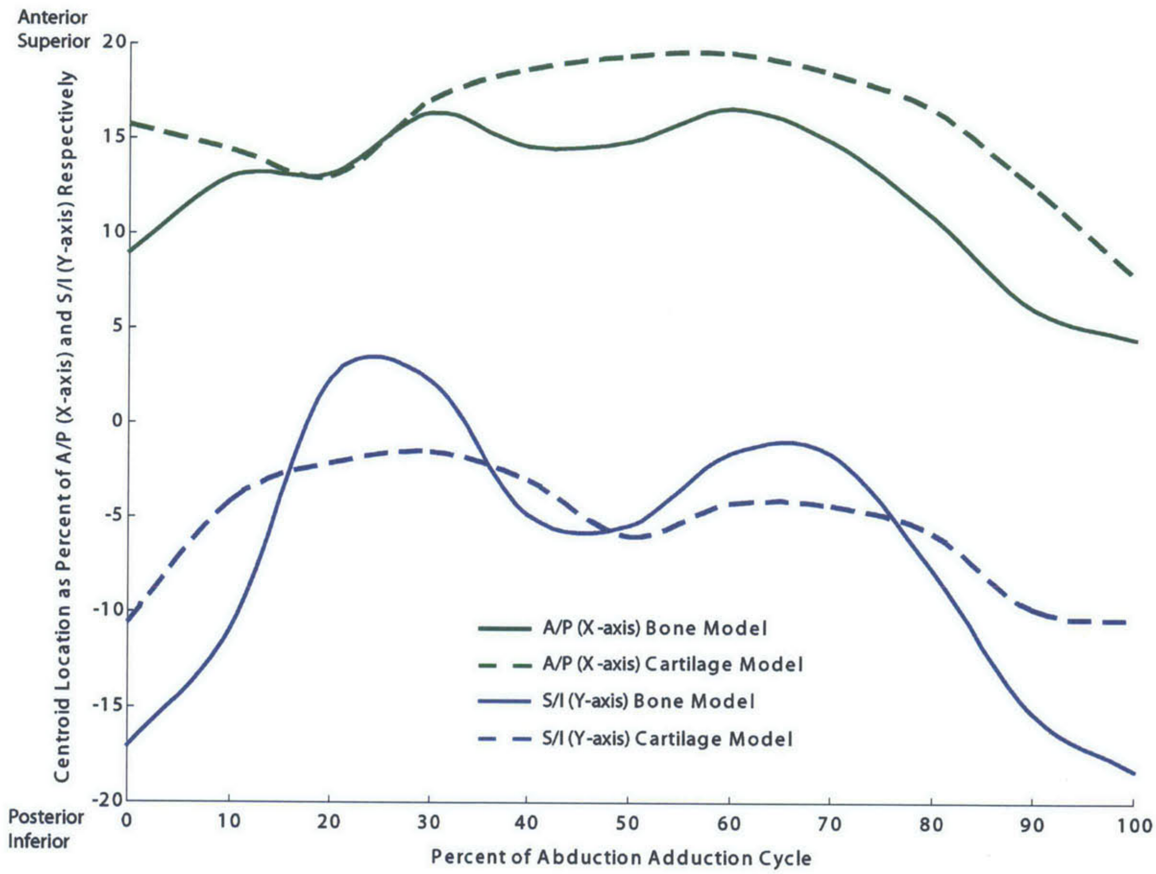

Figure 10 Plots of the average glenohumeral joint contact centroid locations that have been normalized for each subject according to their maximum glenoid cartilage (glenoid scapula bone) dimensions in the anterior/posterior (A/P) and superior/inferior (S/I) directions.

Percent Motion Cycle		0%	10%	20%	30%	40%	50%	60%	70%	80%	90%	100%
Anterior (+) Posterior (-) (X-axis)	Method A	9.0 ± 12.5	13.0 ± 13.7	13.2 ± 15.3	16.4 ± 16.8	14.7 ± 13.6	15.0 ± 14.0	16.7 ± 14.3	15.0 ± 13.9	11.0 ± 9.9	6.1 ± 9.6	4.5 ± 10.9
	Method B	15.7 ± 9.1	14.4 ± 10.0	13.0 ± 13.3	17.1 ± 12.1	18.8 ± 9.4	19.4 ± 10.4	19.6 ± 11.9	18.5 ± 13.2	16.6 ± 13.1	12.5 ± 13.3	7.8 ± 10.7
	P-Value	0.200	0.825	0.965	0.965	0.354	0.402	0.627	0.508	0.233	0.145	0.402
Superior (+) Inferior (-) (Y-axis)	Method A	-17.1 ± 9.2	-10.9 ± 16.1	2.3 ± 13.4	2.2 ± 18.0	-4.9 ± 11.8	-5.4 ± 13.3	-1.5 ± 14.6	-1.6 ± 17.2	-7.7 ± 18.3	-15.3 ± 7.7	-18.3 ± 10.6
	Method B	-10.6 ± 7.3	-4.1 ± 10.4	-2.2 ± 10.9	-1.6 ± 11.4	-3.0 ± 8.7	-6.0 ± 11.5	-4.2 ± 12.0	-4.3 ± 16.2	-5.8 ± 12.3	-9.8 ± 8.5	-10.4 ± 7.5
	P-Value	0.171	0.233	0.508	0.627	0.566	0.895	0.453	0.691	0.691	0.171	0.122

Table 3 The normalized glenohumeral joint contact centroid locations at 10% motion cycle intervals for Method A and Method B, compared with a Mann-Whitney U test. The contact centroid locations are expressed (average ± standard deviation) as a percentage of the maximum A/P (X-axis) and S/I (Y-axis) glenoid cartilage (glenoid scapula bone, rim-to-rim) dimensions.

The A/P (X-axis) contact centroid range of travel for the total motion cycle from method A (without cartilage data) was 21.9 ± 8.3% and from method B (with cartilage data) was 22.3 ± 4.2%. The difference in the A/P contact centroid range of travel between methods A and B was not significant (P = 0.895). However, there was a statistically significant difference (P = 0.012) in the S/I contact centroid range of travel determined from each method. The S/I (Y-axis) contact centroid range of travel for the total motion cycle from method A was 36.6 ± 11.1% and from method B was 23.1 ± 8.2%. In a similar fashion, we found a statistically significant difference (P = 0.038) in the total contact path length determined from method A and from method B. The total contact path length determined from method A was 118.5 ± 23.9% and from method B was 89.8 ± 30.8%.

3.6 *Discussion*

This study successfully (1) describes a technique for quantifying in-vivo glenohumeral joint contact patterns during dynamic shoulder motion utilizing cartilage data (obtained from non-contrast enhanced MRI), (2) quantifies normal glenohumeral joint contact patterns in the young healthy adult during scapular plane abduction adduction motion with external humeral rotation, and (3) compares glenohumeral joint contact patterns determined both with and without articular cartilage data. The results show that the inclusion of articular cartilage data when quantifying in-vivo glenohumeral joint contact patterns has significant effects on the measured overall average A/P contact centroid location, the S/I contact centroid range of travel, and the total contact path length. As a result, the technique presented here offers an advantage over glenohumeral joint contact pattern measurement techniques that neglect articular cartilage data. Similarly, this technique may be more sensitive than traditional 6-DOF glenohumeral joint kinematics (translation and rotation) measurements for the assessment of overall glenohumeral joint health both in the injured joint state and after surgical intervention. Therefore, until proven otherwise, it remains that glenohumeral joint contact patterns must be restored to normal in order to obtain good clinical outcomes after surgical intervention,[36] with a potential benefit of delaying the onset and progression of osteoarthritis. In the future, we hope that this technique is used to objectively quantify the effects that surgical intervention and conservative physical therapy treatment have on restoring in-vivo glenohumeral joint contact patterns to normal for various glenohumeral joint pathologies.

Numerous cadaveric studies[8,10,13,23,36,38] have measured glenohumeral joint contact patterns and have added significant knowledge to the literature. However, caution must be exercised when comparing the glenohumeral joint contact patterns of in-vitro studies to in-vivo studies because cadaveric studies are not yet fully capable of accurately simulating the in-vivo shoulder environment. Nonetheless, Soslowsky et al found that in-vitro glenohumeral joint contact patterns migrated in the posterior-inferior direction on the glenoid from 0 to 120° of scapular plane elevation (abduction).[36] Whereas we found that the contact shifted in the anterior-superior direction with increasing (0 to 110°) scapular plane abduction. One possible explanation to help reconcile this difference is that in Soslowsky et al, the humerus was fixed in $40 \pm 8°$ of external rotation whereas in our study the humerus started (at 0% motion cycle) in $71 \pm 19°$ of external rotation, but with abduction (at 50% motion cycle), the humerus externally rotated to approximately $102 \pm 14°$. Both studies however found contact primarily on the anterior half of the glenoid. This is contrasted by Bey and colleagues that found in-vivo glenohumeral joint contact patterns on the posterior half of the glenoid.[5] Overall, they found contact on the posterior-superior glenoid with abduction motion from 0 to 120° of humerothoracic motion, whereas we found glenohumeral joint contact primarily on anterior-inferior glenoid surface. Three study variations that may help explain this discrepancy are that (1) in the current study, abduction occurred in the scapular plane, whereas in their study, it occured in the coronal plane, (2) in the current study, the humerus was externally rotated, whereas in their study, it was neutrally rotated, and (3) in the current study, the subject age was 26.3 ± 2.4 years, whereas in their study, it was 65.1 ± 10.4 years. Lastly, the control "normal" glenohumeral joint contact patterns reported by Bey et al are actually that of the contralateral asymptomatic (no history of shoulder injury or surgery) shoulder of subjects that underwent rotator cuff tendon repair surgery on their opposite shoulder.[5] Moreover, given that the natural history of rotator cuff tendon disease is to develop slowly and often times unnoticed over many years, it is highly probably that many of the "normal" shoulders had asymptomatic rotator cuff tendon tears (the effect being abnormal shoulder kinematics and consequently abnormal glenohumeral joint contact patterns) and are not actually normal at all.

The contact measurement technique presented in this paper overcomes many of the shortcomings of previous shoulder mechanics quantification methods. However, there are several study design limitations that must be considered. First, our study does not delineate the possible effects that age, gender or strength may have on glenohumeral joint contact patterns. The limited number of enrolled subjects (4 males, 5 females) and young subject age (26.3 ± 2.4 years) precluded this investigation. In addition, we did not examine the possible effects that arm dominance may have on joint contact patterns, as only the dominant (right arm) shoulder was studied. Furthermore, despite previous research that has shown that glenoid orientation influences shoulder mechanics[18,22] and can contribute to component loosening in total shoulder arthroplasty,[26,29,35] the effect of glenoid morphology (anterior-posterior version and superior-inferior tilt) was not assessed relative to the measured contact patterns. On the technical side, a limitation imposed by the DFIS hardware, specifically the mobile C-arm fluoroscopes (BV Pulsera, Philips Medical, USA), was a maximum image acquisition frequency of 30Hz with a 8ms X-ray pulse duration. Image acquisition frequency and X-ray pulse duration directly limit the maximum joint translations and rotations that can be accurately analyzed. For example, the analysis of real-time baseball pitching is outside of the DFIS capabilities. However, the average abduction adduction rotation rate in this study (approximately 55°/s) was well within the systems known capabilities[25] of 180°/s. Another technical limitation imposed by the DFIS was undersized fluoroscopic image intensifiers that precluded the ability to simultaneously acquire images of the humerus, scapula and thoracic landmarks that are necessary to measure scapulothoracic and humerothoracic kinematics. Lastly, the humerus and scapula coordinate systems in this study did not strictly adhere to the recommendations of the ISB.[40] However, the axis directions were similar to those of the ISB, such that, glenohumeral Euler/Cardan angle rotation comparisons can be made to other studies. Though, caution should be exercised when comparing our humerus translation kinematics to other studies, as the scapula reference coordinate system was located at the center of the glenoid and not at the ISB recommended angulus acromialis.

In summary, we have developed a technique for quantifying in-vivo glenohumeral joint articular cartilage contact patterns during dynamic shoulder motion. This technique may be more sensitive than traditional 6-DOF glenohumeral joint kinematics (translation and rotation) measurements for the assessment of overall glenohumeral joint health. We found that by neglecting articular cartilage data during the quantification of glenohumeral joint contact patterns, the total contact path length was overestimated by nearly 30%. Consequently, caution should be exercised when using published glenohumeral joint contact (with and without cartilage data) patterns as the basis for designing wear simulations for total shoulder arthroplasty systems, in effort to not over or under engineer the components. Lastly, we found that in the young healthy adult, during scapular plane abduction adduction motion with external humeral rotation, glenohumeral joint contact was primarily located on the anterior-inferior glenoid surface. This is significant because the majority (approximately

80%) of all shoulder instability occurs in the anterior-inferior direction.[9,14,17,27,30] Therefore, in the future, we hope to use this technique to objectively quantify the glenohumeral joint contact patterns of the unstable shoulder and the consequences that surgery has on altering these patterns. The information learned may help improve clinical outcomes and delay the onset and progression of arthritis.

3.7 *References*

1. Baeyens, J. P.; Van Roy, P.; and Clarys, J. P.: Intra-articular kinematics of the normal glenohumeral joint in the late preparatory phase of throwing: Kaltenborn's rule revisited. *Ergonomics,* 43(10): 1726-37, 2000.

2. Baeyens, J. P.; Van Roy, P.; De Schepper, A.; Declercq, G.; and Clarijs, J. P.: Glenohumeral joint kinematics related to minor anterior instability of the shoulder at the end of the late preparatory phase of throwing. *Clin Biomech (Bristol, Avon),* 16(9): 752-7, 2001.

3. Balg, F.; Boulianne, M.; and Boileau, P.: Bicipital groove orientation: considerations for the retroversion of a prosthesis in fractures of the proximal humerus. *J Shoulder Elbow Surg,* 15(2): 195-8, 2006.

4. Beaulieu, C. F.; Hodge, D. K.; Bergman, A. G.; Butts, K.; Daniel, B. L.; Napper, C. L.; Darrow, R. D.; Dumoulin, C. L.; and Herfkens, R. J.: Glenohumeral relationships during physiologic shoulder motion and stress testing: initial experience with open MR imaging and active imaging-plane registration. *Radiology,* 212(3): 699-705, 1999.

5. Bey, M.; Kline, S.; Zauel, R.; Kolowich, P.; and Lock, T.: In Vivo Measurement of Glenohumeral Joint Contact Patterns. *EURASIP Journal on Advances in Signal Processing,* doi:10.1155/2010/162136: 6 pages, 2010.

6. Bey, M. J.; Kline, S. K.; Zauel, R.; Lock, T. R.; and Kolowich, P. A.: Measuring dynamic in-vivo glenohumeral joint kinematics: Technique and preliminary results. *J Biomech,* 41(3): 711-4, 2008.

7. Bey, M. J.; Zauel, R.; Brock, S. K.; and Tashman, S.: Validation of a new model-based tracking technique for measuring three-dimensional, in vivo glenohumeral joint kinematics. *J Biomech Eng,* 128(4): 604-9, 2006.

8. Creighton, R. A.; Cole, B. J.; Nicholson, G. P.; Romeo, A. A.; and Lorenz, E. P.: Effect of lateral meniscus allograft on shoulder articular contact areas and pressures. *J Shoulder Elbow Surg,* 16(3): 367-72, 2007.

9. Dodson, C. C., and Cordasco, F. A.: Anterior glenohumeral joint dislocations. *Orthop Clin North Am,* 39(4): 507-18, vii, 2008.

10. Ghodadra, N.; Gupta, A.; Romeo, A. A.; Bach, B. R., Jr.; Verma, N.; Shewman, E.; Goldstein, J.; and Provencher, M. T.: Normalization of glenohumeral articular

contact pressures after Latarjet or iliac crest bone-grafting. *J Bone Joint Surg Am,* 92(6): 1478-89, 2010.

11. Graichen, H.; Hinterwimmer, S.; von Eisenhart-Rothe, R.; Vogl, T.; Englmeier, K. H.; and Eckstein, F.: Effect of abducting and adducting muscle activity on glenohumeral translation, scapular kinematics and subacromial space width in vivo. *J Biomech,* 38(4): 755-60, 2005.

12. Greis, P. E.; Scuderi, M. G.; Mohr, A.; Bachus, K. N.; and Burks, R. T.: Glenohumeral articular contact areas and pressures following labral and osseous injury to the anteroinferior quadrant of the glenoid. *J Shoulder Elbow Surg,* 11(5): 442-51, 2002.

13. Gupta, R., and Lee, T. Q.: Positional-dependent changes in glenohumeral joint contact pressure and force: possible biomechanical etiology of posterior glenoid wear. *J Shoulder Elbow Surg,* 14(1 Suppl S): 105S-110S, 2005.

14. Hovelius, L.: The natural history of primary anterior dislocation of the shoulder in the young. *J Orthop Sci,* 4(4): 307-17, 1999.

15. Hromadka, R.; Kubena, A. A.; Pokorny, D.; Popelka, S.; Jahoda, D.; and Sosna, A.: Lesser tuberosity is more reliable than bicipital groove when determining orientation of humeral head in primary shoulder arthroplasty. *Surg Radiol Anat,* 32(1): 31-7, 2010.

16. Inman, V. T.; Saunders, J. B.; and Abbott, L. C.: Observations on the function of the shoulder joint. *J Bone Joint Surg Am,* 26(1): 1-30, 1944.

17. Itoi, E.; Lee, S. B.; Amrami, K. K.; Wenger, D. E.; and An, K. N.: Quantitative assessment of classic anteroinferior bony Bankart lesions by radiography and computed tomography. *Am J Sports Med,* 31(1): 112-8, 2003.

18. Kandemir, U.; Allaire, R. B.; Jolly, J. T.; Debski, R. E.; and McMahon, P. J.: The relationship between the orientation of the glenoid and tears of the rotator cuff. *J Bone Joint Surg Br,* 88(8): 1105-9, 2006.

19. Keenan, K. E.; Besier, T. F.; Pauly, J. M.; Han, E.; Rosenberg, J.; Smith, R. L.; Delp, S. L.; Beaupre, G. S.; and Gold, G. E.: Prediction of glycosaminoglycan content in human cartilage by age, T1rho and T2 MRI. *Osteoarthritis Cartilage,* 19(2): 171-9, 2011.

20. Kon, Y.; Nishinaka, N.; Gamada, K.; Tsutsui, H.; and Banks, S. A.: The influence of handheld weight on the scapulohumeral rhythm. *J Shoulder Elbow Surg,* 17(6): 943-6, 2008.

21. Kummer, F. J.; Perkins, R.; and Zuckerman, J. D.: The use of the bicipital groove for alignment of the humeral stem in shoulder arthroplasty. *J Shoulder Elbow Surg,* 7(2): 144-6, 1998.

22. Lewis, G. S., and Armstrong, A. D.: Glenoid spherical orientation and version. *J Shoulder Elbow Surg,* 20(1): 3-11, 2011.

23. Lin, T.; Javidan, P.; McGarry, M. H.; Gonzalez-Lomas, G.; Limpisvasti, O.; and Lee, T. Q.: Glenohumeral contact pressure in a simulated active compression test using cadaveric shoulders. *J Shoulder Elbow Surg,* 22(3): 365-74, 2013.

24. Mandalidis, D. G.; Mc Glone, B. S.; Quigley, R. F.; McInerney, D.; and O'Brien, M.: Digital fluoroscopic assessment of the scapulohumeral rhythm. *Surg Radiol Anat,* 21(4): 241-6, 1999.

25. Massimini, D. F.; Warner, J. J.; and Li, G.: Non-invasive determination of coupled motion of the scapula and humerus-An in-vitro validation. *J Biomech,* 44(3): 408-12, 2011.

26. Matsen, F. A., 3rd; Clinton, J.; Lynch, J.; Bertelsen, A.; and Richardson, M. L.: Glenoid component failure in total shoulder arthroplasty. *J Bone Joint Surg Am,* 90(4): 885-96, 2008.

27. Matsen, F. A., 3rd, and Thomas, S. T.: Glenohumeral Instability. In *Surgery of the Musculoskeletal System*, pp. 1439-1469. Edited by Evarts, C. M., 1439-1469, New York, Churchill Livingstone, 1990.

28. Menezes, N. M.; Gray, M. L.; Hartke, J. R.; and Burstein, D.: T2 and T1rho MRI in articular cartilage systems. *Magn Reson Med,* 51(3): 503-9, 2004.

29. Nyffeler, R. W.; Sheikh, R.; Atkinson, T. S.; Jacob, H. A.; Favre, P.; and Gerber, C.: Effects of glenoid component version on humeral head displacement and joint reaction forces: an experimental study. *J Shoulder Elbow Surg,* 15(5): 625-9, 2006.

30. Owens, B. D.; Duffey, M. L.; Nelson, B. J.; DeBerardino, T. M.; Taylor, D. C.; and Mountcastle, S. B.: The incidence and characteristics of shoulder instability at the United States Military Academy. *Am J Sports Med,* 35(7): 1168-73, 2007.

31. Pfirrmann, C. W.; Huser, M.; Szekely, G.; Hodler, J.; and Gerber, C.: Evaluation of complex joint motion with computer-based analysis of fluoroscopic sequences. *Invest Radiol,* 37(2): 73-6, 2002.

32. Sahara, W.; Sugamoto, K.; Murai, M.; Tanaka, H.; and Yoshikawa, H.: 3D kinematic analysis of the acromioclavicular joint during arm abduction using vertically open MRI. *J Orthop Res,* 24(9): 1823-31, 2006.

33. Sans, N. et al.: Kinematic MR imaging of the shoulder: normal patterns. *AJR Am J Roentgenol,* 167(6): 1517-22, 1996.

34. Senk, M., and Cheze, L.: Rotation sequence as an important factor in shoulder kinematics. *Clin Biomech (Bristol, Avon),* 21 Suppl 1: S3-8, 2006.

35. Shapiro, T. A.; McGarry, M. H.; Gupta, R.; Lee, Y. S.; and Lee, T. Q.: Biomechanical effects of glenoid retroversion in total shoulder arthroplasty. *J Shoulder Elbow Surg,* 16(3 Suppl): S90-5, 2007.

36. Soslowsky, L. J.; Flatow, E. L.; Bigliani, L. U.; Pawluk, R. J.; Ateshian, G. A.; and Mow, V. C.: Quantitation of in situ contact areas at the glenohumeral joint: a biomechanical study. *J Orthop Res,* 10(4): 524-34, 1992.

37. Tokuda, O.; Kunihiro, Y.; and Matsunaga, N.: Kinematic MRI of the normal shoulder using a specially designed positioning device. *J Comput Assist Tomogr,* 26(5): 849-54, 2002.

38. Warner, J. J.; Bowen, M. K.; Deng, X. H.; Hannafin, J. A.; Arnoczky, S. P.; and Warren, R. F.: Articular contact patterns of the normal glenohumeral joint. *J Shoulder Elbow Surg,* 7(4): 381-8, 1998.

39. Wong, C. S.; Yan, C. H.; Gong, N. J.; Li, T.; Chan, Q.; and Chu, Y. C.: Imaging biomarker with T1rho and T2 mappings in osteoarthritis - in vivo human articular cartilage study. *Eur J Radiol,* 82(4): 647-50, 2013.

40. Wu, G. et al.: ISB recommendation on definitions of joint coordinate systems of various joints for the reporting of human joint motion--Part II: shoulder, elbow, wrist and hand. *J Biomech,* 38(5): 981-992, 2005.

41. Zhu, Z.; Massimini, D. F.; Wang, G.; Warner, J. J.; and Li, G.: The accuracy and repeatability of an automatic 2D-3D fluoroscopic image-model registration technique for determining shoulder joint kinematics. *Med Eng Phys*, 2012.

Chapter 4: Application - Nerve Tracking

4.1 Preface

In chapter 4, I will apply the validated bone model tracking technique for measuring dynamic shoulder joint kinematics described in chapter 2, to a clinical relevant shoulder joint injury and surgical intervention model. In the process, I describe a novel method for tracking nerves (soft tissue) in 6-DOF during dynamic simulated shoulder joint motion in a cadaveric model. This is the first study (ever) to dynamically track a nerve in 6-DOF relative to bony anatomic landmarks; the results give scientists and clinicians insight into the process of nerve injury by traction (stretch) and the effects subsequent to surgical intervention.

The text and figures contained in chapter 4 are directly copied from the Elsevier published journal article shown in the journal header below and formatted for the MIT thesis guidelines. As an author of this article, Elsevier grants me (an author) an unrestricted license to reuse my previous published work in my (the author's) thesis. No transfer of copyright is required between the authors, Elsevier and the Massachusetts Institute of Technology.

J Shoulder Elbow Surg (2013) 22, 463-470

ELSEVIER

Journal of Shoulder and Elbow Surgery

www.elsevier.com/locate/ymse

Suprascapular nerve anatomy during shoulder motion: a cadaveric proof of concept study with implications for neurogenic shoulder pain

Daniel F. Massimini, SM[a,b], Anshu Singh, MD[a], Jessica H. Wells, BA[a], Guoan Li, PhD[a], Jon JP. Warner, MD[a,]*

[a]*Bioengineering Laboratory, Massachusetts General Hospital, Harvard Medical School, Boston, MA, USA*
[b]*Department of Mechanical Engineering, Massachusetts Institute of Technology, Cambridge, MA, USA*

4.2 Abstract

Background: The suprascapular nerve (SSN) carries sensory fibers which may contribute to shoulder pain. Prior anatomic study demonstrated that alteration in SSN course with simulated rotator cuff tendon (RCT) tears cause tethering and potential traction injury to the nerve at the suprascapular notch. Because the SSN has been implicated as a major source of pain with RCT tearing, it is critical to understand nerve anatomy during shoulder motion. We hypothesized that we could evaluate the SSN course with a novel technique to evaluate effects of simulated RCT tears, repair, and/or release of the nerve.

Methods: The course of the SSN was tracked with a dual fluoroscopic imaging system in a cadaveric model with simulated rotator cuff muscle forces during dynamic shoulder motion.

Results: After a simulated full-thickness supraspinatus/infraspinatus tendon tear, the SSN translated medially 3.5mm at the spinoglenoid notch compared to the anatomic SSN course. Anatomic footprint repair of these tendons restored the SSN course to normal. Open release of the transverse scapular ligament caused the SSN to move 2.5mm superior-posterior out of the suprascapular notch.

Conclusion: This pilot study demonstrated that the dynamic SSN course can be evaluated and may be altered by a RCT tear. Preliminary results suggest release of the transverse scapular ligament allowed the SSN to move upward out of the notch. This provides a biomechanical proof of concept that SSN traction neuropathy may occur with RCT tears and that release of the transverse scapular ligament may alleviate this by altering the course of the nerve.

4.3 *Introduction*

Recent clinical research has demonstrated that suprascapular nerve (SSN) dysfunction may occur in patients with rotator cuff tendon tears.[4,6,18] Moreover, experimental anatomic dissection studies have implicated tethering of the SSN at the suprascapular notch as a potential pain generator with retration of the supraspinatus muscle.[2,11] Hence, the inherent anatomy of the SSN makes it susceptible to compression and/or traction injury in association with rotator cuff tendon tears. Additionally, a further risk factor may be the variable anatomy of the suprascapular notch; from a deep, narrow notch with an ossified transverse scapular ligament, to no discrete notch at all.[8,15]

The SSN originates from the C5 and C6 nerve roots (with contribution from C4 in some individuals), and courses through the suprascapular notch and into the supraspinatus fossa, underneath the supraspinatus muscle, and abruptly changes course around the spine of the scapula at the spinoglenoid notch as it forms 2-4 motor branches to the infraspinatus.[11,26,28] As such, if the supraspinatus and infraspinatus tendons retract medially with a tendon tear, then the SSN will be vulnerable to a traction injury.[6] Albritton et al verified this theory using a simulated rotator cuff tendon tear model. They found that with a simulated rotator cuff tendon tear, the SSN was pulled medially and tethered at the suprascapular notch, suggesting that the SSN may be at risk of traction along its course on the scapula.[2]

Suprascapular neuropathy is usually diagnosed by both physical examination and electrodiagnostic study of the shoulder.[3] Literature regarding this entity has increased significantly in the last decade. The increased incidence of suprascapular neuropathy is likely based on awareness amongst clinicians of the common causes: paralabral cysts adjacent to the spinoglenoid notch,[1,9,24,29] mass effect,[14,30] traction during high level overhead sport,[10,17,22] scapular fracture,[5] iatrogenic injury,[27] and traction from a retracted rotator cuff tendon with resulting fatty infiltration of the posterosuperior rotator cuff.[6,18]

Treatment for suprascapular neuropathy has traditionally involved open release, and, more recently, arthroscopic release of the transverse scapular ligament. This approach is based on the assumption that the nerve course is altered in the diseased state, and that traction is relieved by surgical release. A 2007 cadaveric study by Plancher et al demonstrated that arthroscopic release of the spinoglenoid ligament directly relieved pressure on the distal suprascapular nerve motor branch.[21] Despite the recent enthusiasm for suprascapular nerve pathology, significant controversy remains regarding the precise mechanism and location of nerve injury caused by massive rotator cuff tendon tears, and the mechanism by which transverse scapular ligament release appears to relieve this inciting trauma.

The purposes of our proof of concept pilot study are (1) to evaluate a validated 3-dimensional (3D) fluoroscopic imaging technique[19] to empirically model the anatomic course of the SSN during shoulder motion, and (2) to evaluate the SSN course with and without a simulated rotator cuff tendon tear and its repair in a cadaver model and/or with the effect of release of the transverse scapular ligament. We hypothesized that this novel model could evaluate the SSN to determine if it would be subject to traction at the suprascapular notch and that the change in orientation and position of the nerve with a simulated rotator cuff tear would increase the likelihood of traction on the nerve at this location as well as at the spinoglenoid notch. Our secondary hypothesis was that repair of the tendons would restore anatomy of the nerve to normal and that the release of the transverse scapular ligament would result in elimination of traction of the nerve at the suprascapular notch by altering its course.

4.4 *Materials and Method*

Specimen Preparation

One male fresh-frozen cadaver torso (age 30) with upper extremities intact and cephalus removed cranial to the C5 vertebrae was acquired. The specimen was stored at minus 4°F until thawed at room temperature for data acquisition. To provide fixed radio-opaque markers to assist bony tracking, titanium spheres 1/8" in diameter were implanted within the cortical shell of the scapula and humerus of the right shoulder. All dissections and operations were performed by a fellowship-trained orthopaedic shoulder surgeon (A.S). For the humerus, a limited deltopectoral approach was utilized to directly visualize the lateral aspect of the humeral head. Five spheres were uniformly implanted into the lateral cortical bone of the humeral head and away from the articular surface. For the scapula, a posterior approach was utilized along the scapular spine. One sphere was implanted into the lateral acromion, three spheres along the scapular spine, and one sphere near the spinoglenoid notch. The cadaver was noted to have a typical U-shaped suprascapular notch with a non-ossified ligament.

To mark the SSN and its terminal branches, seven tungsten wires (OD = 0.025") and one tungsten wire (OD = 0.045"), all 0.160" in length were inserted coaxially into the SSN and along its course in select accessible locations of interest. Utilizing the existing posterior approach along the scapular spine, the SSN was directly visualized at select locations of interest from proximal to the suprascapular notch to the terminal motor branches. An attempt was made to minimize disruption of native adhesions to surrounding fat, muscle, and bone to minimize alteration of nerve kinematics. To this end, less than 5mm of nerve had to be visualized for each insertion, as an angiocatheder was inserted coaxially into the nerve, and the tungsten wires inserted centrally. Small barbs on each end of the wires served to prevent pistoning or toggle from their initial position. A running locking stitch was used to close the deltopectoral and posterior approaches. Wire locations relative to the SSN anatomy are shown in Figure 11.

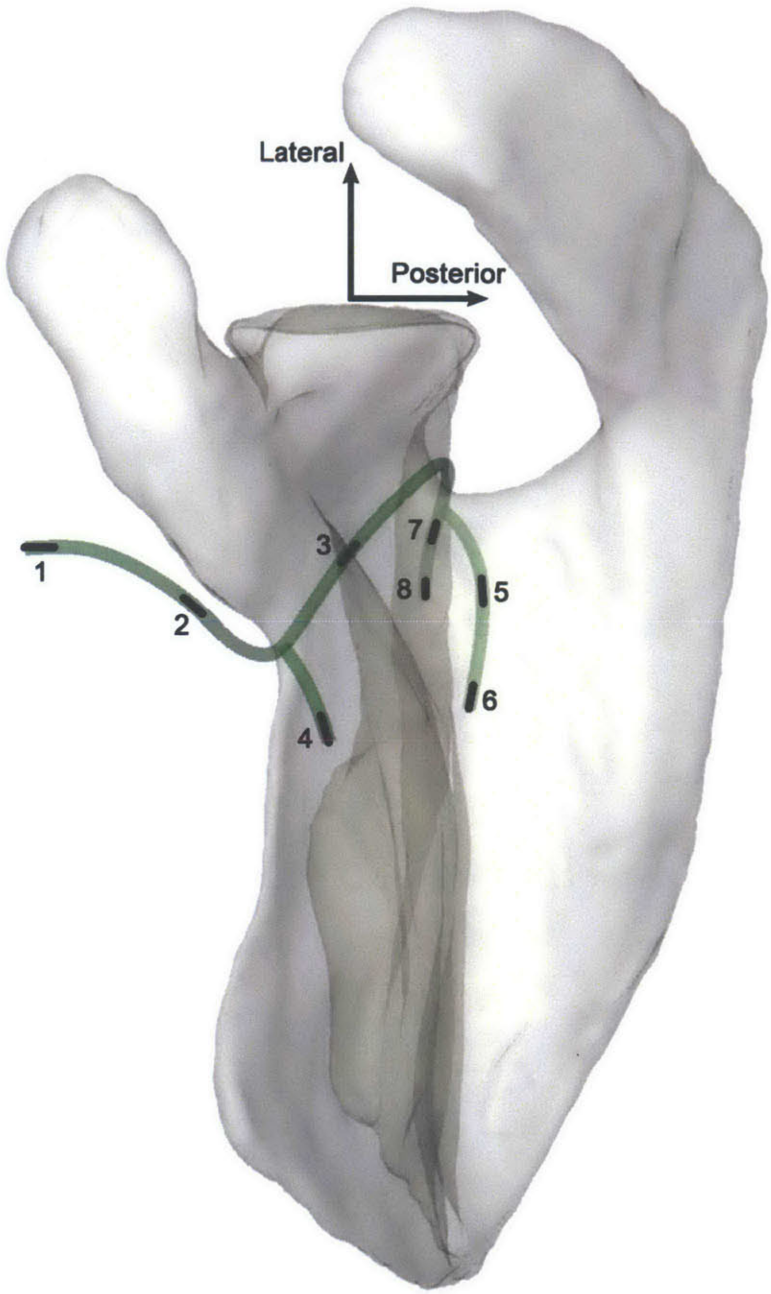

Figure 11 A top view of the scapula model with the tungsten wire placement and numerical assignment within the SSN course relative to the scapula used for 3D SSN course constructions in the virtual environment.

Bone Model Reconstruction

The specimen underwent high resolution computer tomography in a LightSpeed Pro 16 (GE Healthcare, Little Chalfont, Bucks, UK) with axial slices spaced 0.625mm. The image resolution was 512 by 512 pixels with a field of view of 280 by 420mm. DICOM images of the scan were transferred to a personal computer and automatically segmented by a custom MATLAB (The Mathworks Inc, Natick, MA, USA) script based on the intensity gradient of each pixel. The segmented contours were transferred into the Rhinoceros 3D v4.0 program (Robert McNeel & Associates, Seattle, WA, USA) and B-Splines were meshed to create 3D surface models of the scapula and humerus.

Testing Protocol

The specimen was rigidly secured to a custom apparatus via pedicle screws through the spine. The right shoulder was placed with the glenohumeral joint centered in the imaging volume created by the dual fluoroscopic imaging system (DFIS) (Figure 12). This configuration allowed for unconstrained scapulothoracic motion.

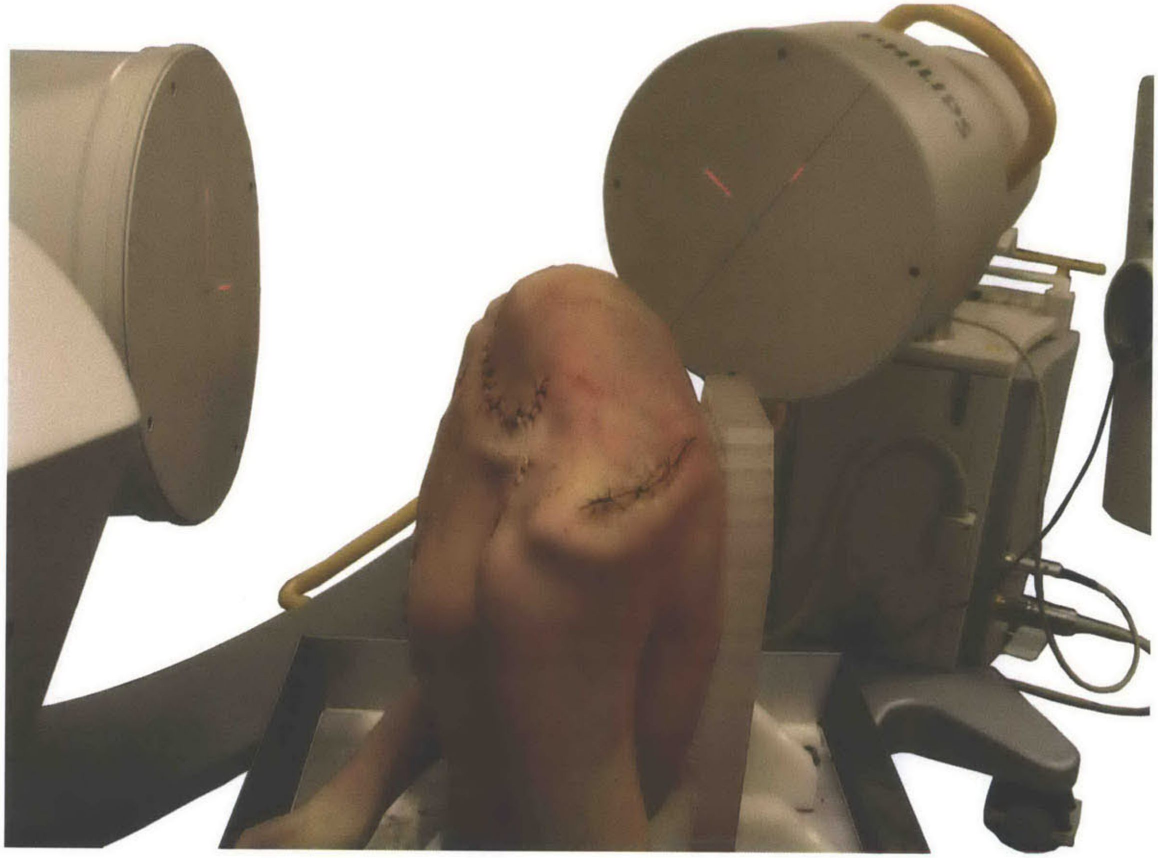

Figure 12 A photograph of the DFIS with cadaver specimen mounted to a custom fixation apparatus. The photo was taken before muscle loads were applied to the rotator cuff. The testing room background has been whited out for clarity.

Native rotator cuff muscle forces were modeled after a 2003 Mayo Clinic cadaveric study of rotator cuff tendon tears by Mura et al.[20] Separate #5 Fiberwire sutures (Fiberwire, Arthrex Inc., Naples, FL. USA) were sewn into the native musculotendinous junction of each rotator cuff muscle, with two sutures in the subscapularis due to its large superior to inferior breath. Heavy gauge nylon rope was tied to each individual Fiberwire and passed through a custom jig to mimic the force vectors of in-vivo muscles according to their cross sectional area and direction of pull. The simulated muscle forces were: subscapularis 30N, supraspinatus 16N, infraspinatus 20N and teres minor 12N. The shoulder was grossly well balanced after tensioning.

Simultaneous fluoroscopic images of the right shoulder were acquired at 30 frames per second with an 8ms pulse width while the arm was manually manipulated in cycles of 0°-130°-0° abduction/adduction in the scapular plane at a rotation rate of approximately 45°/s. Five configurations were simulated in the following sequence: (case #1) intact rotator cuff; (case #2) an acute simulated full-thickness infraspinatus/supraspinatus tendon tear; (case #3) a transosseous double row repair of the tendons; (case #4) an acute simulated full-thickness infraspinatus/supraspinatus tendon tear with transection of the transverse scapular ligament; and (case #5) a transosseous double row repair of the tendons with transection of the transverse scapular ligament.

For case #2, the simulated rotator cuff tendon tear was effectuated with a #11 blade at the tendinous insertion of the superior cuff onto the greater tuberosity via the deltopectoral interval. The native footprint of both the supraspinatus and infraspinatus were both sharply incised.[7] Open rotator cuff tendon repair was performed through the deltopectoral interval with internal rotation of the arm. The goal of repair was to accurately restore the native resting length of the tendon using soft tissue landmarks made during creation of the simulated tear. Three 1cm wide mattress sutures with #5 Fiberwire were placed at the medial edge of the tuberosity and tied on the bursal aspect of the cuff. Two additional simple lateral row sutures were placed on the lateral aspect of the greater tuberosity to reduce the supraspinatus and infraspinatus tendons to their anatomic footprints and to minimize abrasion throughout the range of motion.

Dual Fluoroscopic Imaging System (DFIS): 3D Kinematics

The system consists of two fluoroscopes (12" BV Pulsera, Phillips Medical, USA) arranged with the image intensifiers at approximately 120° to one another. The accuracy of the tracking system was ±0.3mm in translation and ±0.5° in rotation.[19] The nominal fluoroscope settings were 5.0mA and 55kV. The acquired fluoroscopic images were transferred to a personal computer and corrected for geometric distortion. A modified Gronenschild,[12,13] global surface mapping technique was utilized. Within solid modeling software (Rhinoceros 3D v4.0, Robert McNeel & Associates, Seattle, WA, USA) a virtual DFIS was created to reproduce the physical geometry of the DFIS. Corrected fluoroscopic image pairs and 3D surface models of the scapula and humerus were imported into the virtual DFIS. The position of the scapula and humerus were adjusted in 6-DOF so that the 3D surface model spheres aligned with the intersection of the vectors projected from the spheres on the fluoroscopic images, as a result, the 3D positions of the scapula and humerus were recreated (Figure 13). Bone kinematics were reproduced in approximately 0.33 second intervals (15 image pairs/poses per configuration) for the total abduction/adduction cycle for each configuration tested.

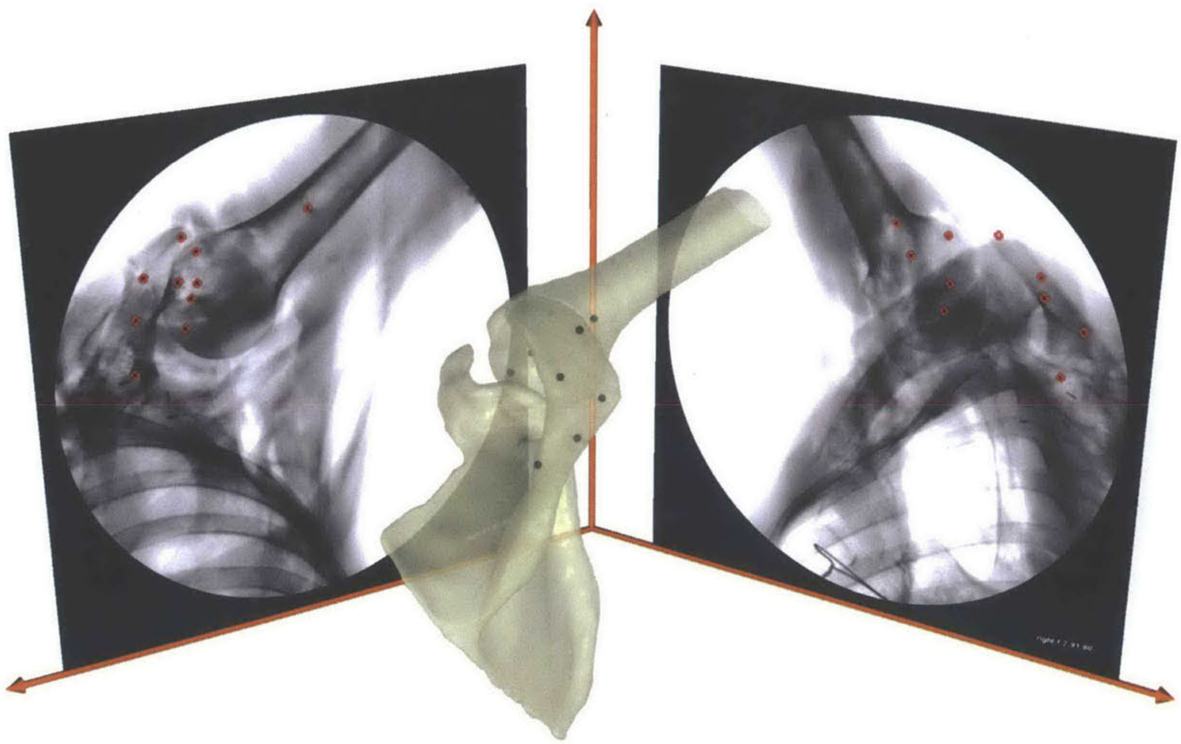

Figure 13 A rendering from solid modeling software of the virtual DFIS with reproduced 3D bone model kinematics from alignment of the spheres within the models to the fluoroscopic image pairs.

DFIS: Dynamic SSN Tracking

The SSN was tracked by reproducing the position of the implanted tungsten wires in the virtual DFIS. Each tungsten wire's position was reproduced by constructing vectors from the virtual fluoroscopic source to the wire ends in the fluoroscopic images on the virtual fluoroscopic image planes. The intersection of corresponding vectors from the two image planes identified the 3D position of the wire ends in the virtual DFIS (Figure 14). Corresponding wire ends were connected with a line to reproduce the position of the implanted tungsten wire in the virtual DFIS. In this manner, all wire ends and wire positions were found and manually checked by two investigators for each fluoroscopic image pair (15 image pairs/poses per configuration) for which bone kinematics were reproduced.

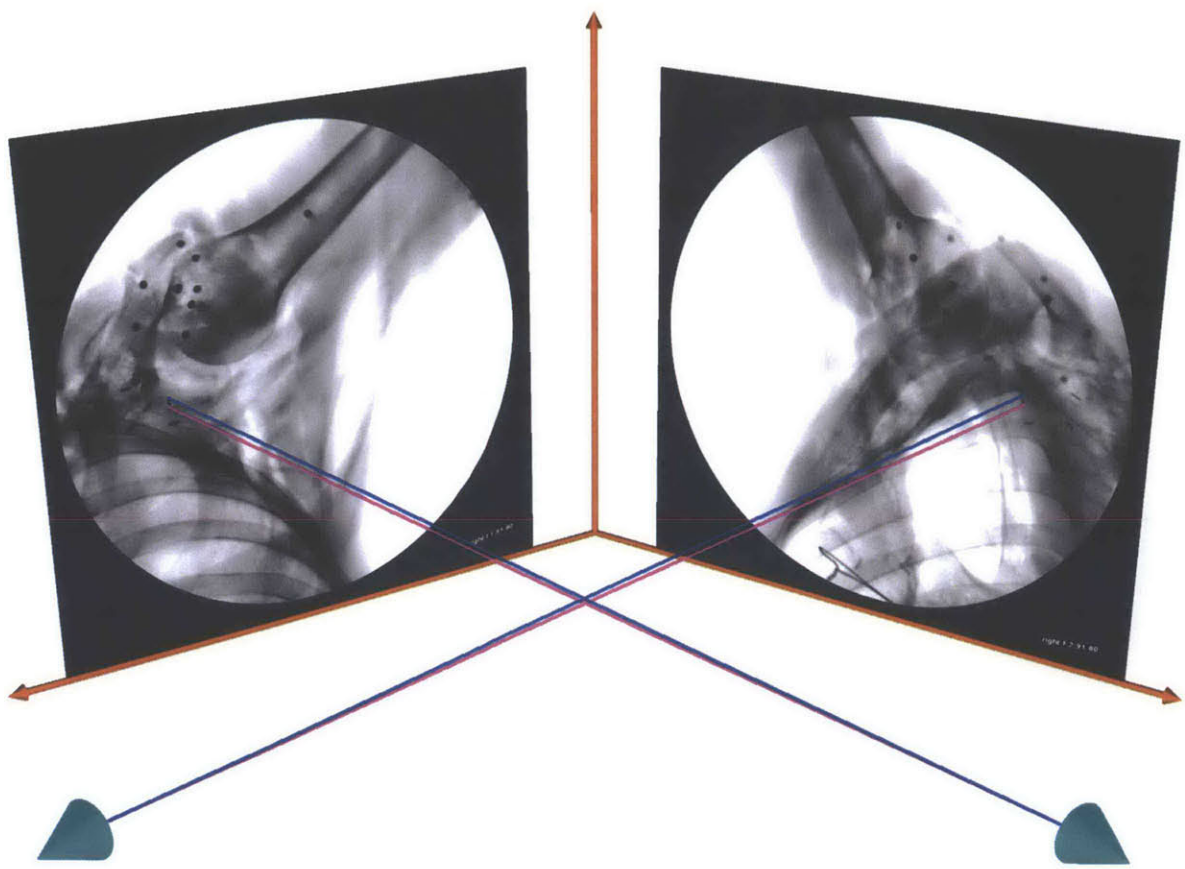

Figure 14 A rendering from solid modeling software of the virtual DFIS with vector projections illustrating the technique used to orient the tungsten wires in the virtual environment for SSN course construction.

For each configuration tested (5 total), the positions of the tungsten wires relative to the scapula at each pose (15 poses per configuration) were used to find the average position of each wire over the abduction/adduction cycle. A 3D curve was fit through the average tungsten wire positions in the virtual DFIS to recreate the average course of the SSN during the simulated 0°-130°-0° abduction/adduction cycle in the scapular plane. The SSN courses for the five configurations tested were overlaid on the scapula for qualitative and quantitative assessment. Each SSN course was visually represented by a color coded 1.5mm diameter tube in the final 3D model (Figures 15-18).

Proof of Concept

This pilot study was designed to determine whether we could biomechanically evaluate the SSN course with and without a simulated rotator cuff tendon tear and its repair in a cadaveric model using a highly accurate and validated DFIS methodology. The accuracy of the position of each tungsten wire was measured to ±0.3mm, whereas the measured range of SSN translation between configurations was 2.5-3.5mm. Accordingly, the magnitude of measured nerve translations compared to the accuracy of the tracking system supports the analysis of one cadaver shoulder to (1) show the technical feasibility of nerve tracking with DFIS during dynamic motion in a cadaveric model, and (2) demonstrate the concept that SSN anatomy may be empirically altered by a rotator cuff tendon tear and/or with release of the transverse scapular ligament.

4.5 Results

Case #1 - intact rotator cuff

An illustration of the anatomic SSN course is shown in Figure 15.

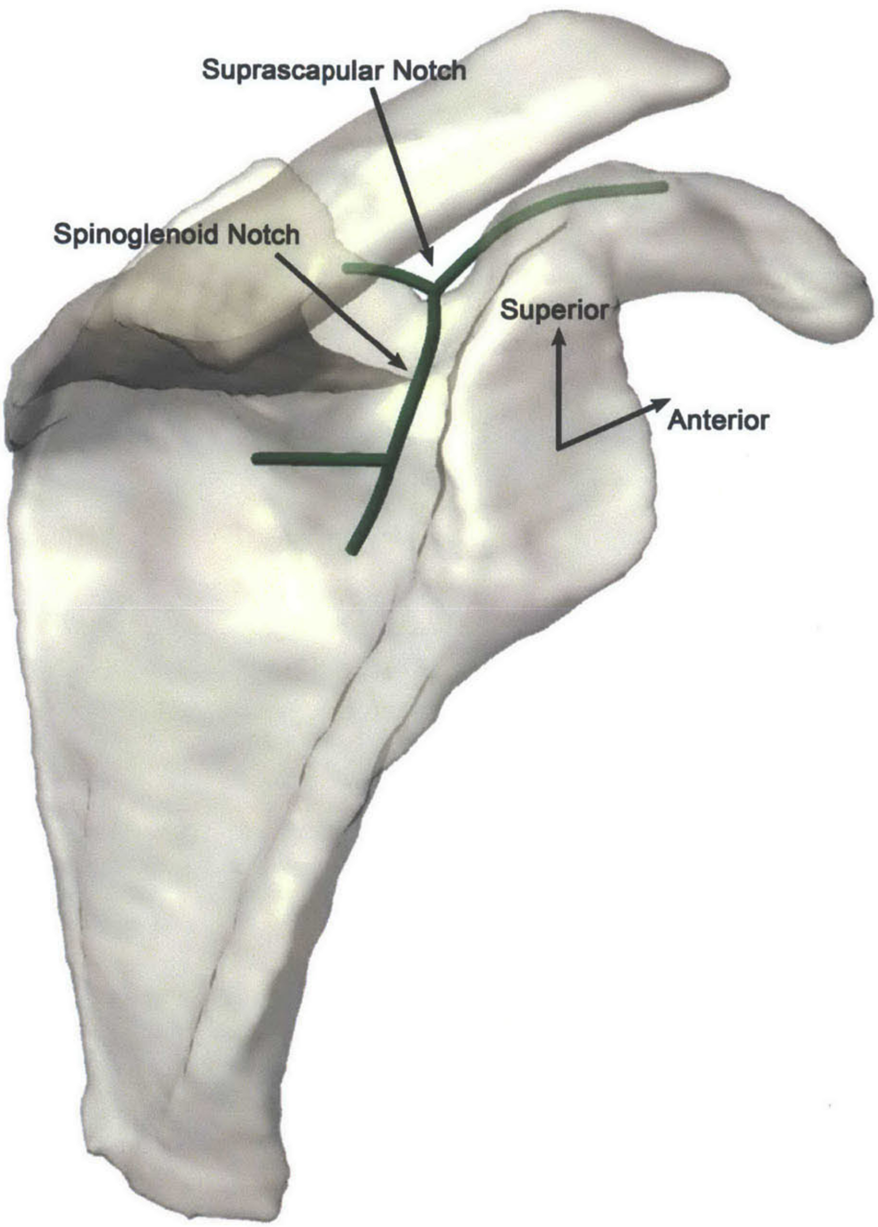

Figure 15 A posteriolateral view illustration of the scapula identifying the suprascapular and spinoglenoid notches. The green nerve course shown is that of the anatomic SSN with an intact rotator cuff.

Case #2 - acute simulated full-thickness infraspinatus/supraspinatus tendon tear

The SSN translated medially 3.5mm at the spinoglenoid notch compared to the anatomic SSN course (case #1). No change in the nerve course was observed at the suprascapular notch. An illustration of these nerve motions is shown in Figure 16.

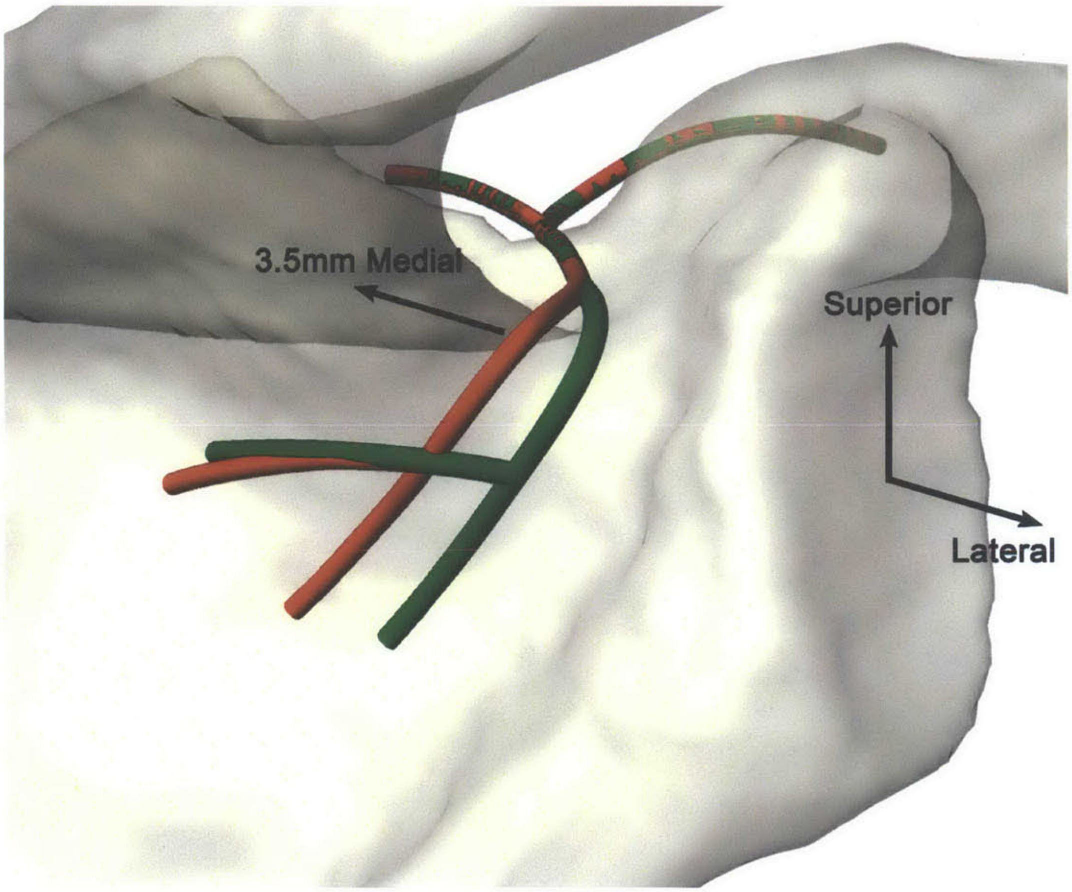

Figure 16 A posteriolateral view illustration of the anatomic SSN with an intact rotator cuff shown in green (case #1). Shown in red is the SSN course with an acute simulated full-thickness infraspinatus/supraspinatus tendon tear (case #2).

Case #3 - transosseous double row repair of the tendons

The SSN translated laterally 3.5mm at the spinoglenoid notch compared to the simulated full-thickness tendon tear (case #2), effectively restoring the anatomic nerve course at the spinoglenoid notch (Figure 15, representing both case #1 and case #3). No change in the nerve course was observed at the suprascapular notch.

Case #4 - acute simulated full-thickness infraspinatus/supraspinatus tendon tear with transection of the transverse scapular ligament

The SSN translated medially 3.5mm at the spinoglenoid notch and 2.5mm superior-posterior at the suprascapular notch compared to the anatomic SSN course (case #1). An illustration of these nerve motions are shown in Figure 17.

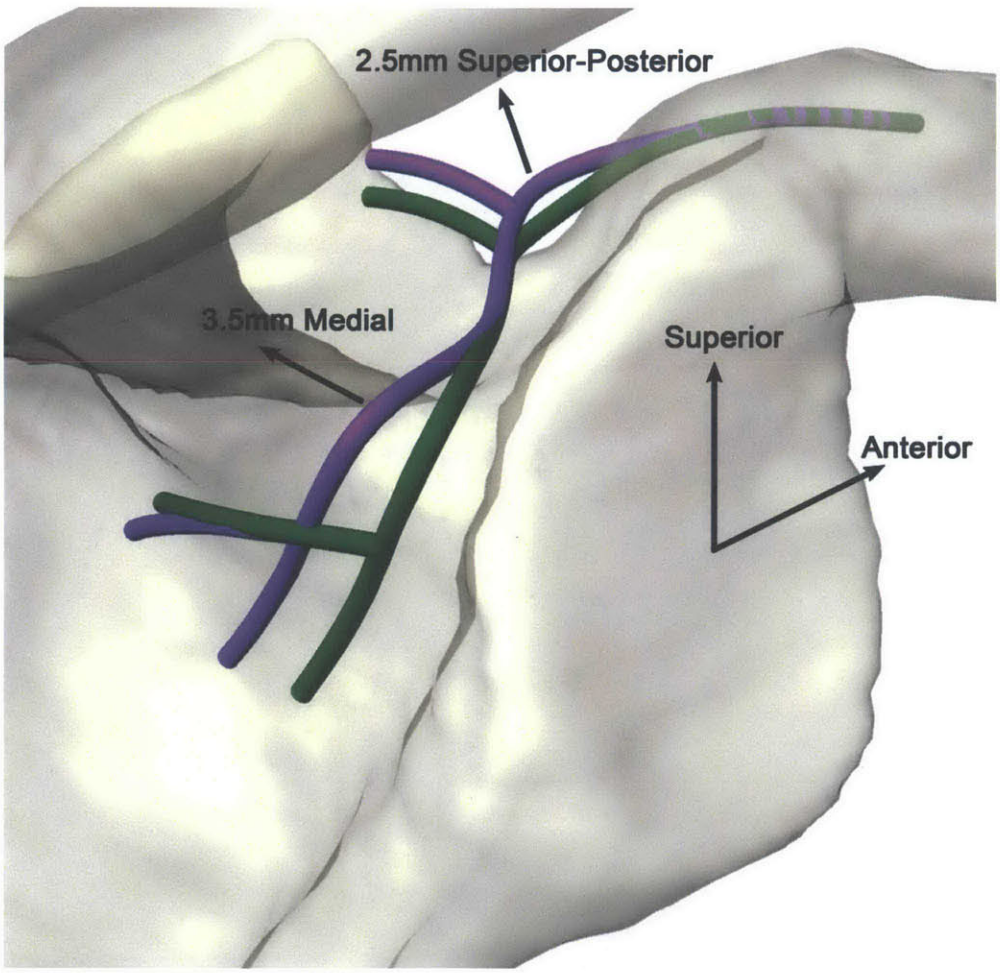

Figure 17 A posteriolateral view illustration of the anatomic SSN with an intact rotator cuff shown in green (case #1). Shown in purple is the SSN course with an acute simulated full-thickness infraspinatus/supraspinatus tendon tear with transaction of the transverse scapular ligament (case #4)

Case #5 - transosseous double row repair of the tendons with transection of the transverse scapular ligament

The SSN translated 2.5mm superior-posterior at the suprascapular notch while no change in the nerve course was observed at the spinoglenoid notch compared to the anatomic SSN course (case #1). Effectively, the rotator cuff tendon repair restored the anatomic nerve course at the spinoglenoid notch, while transection of the transverse scapular ligament allowed a more direct or shorter nerve path at the suprascapular notch (Figure 18).

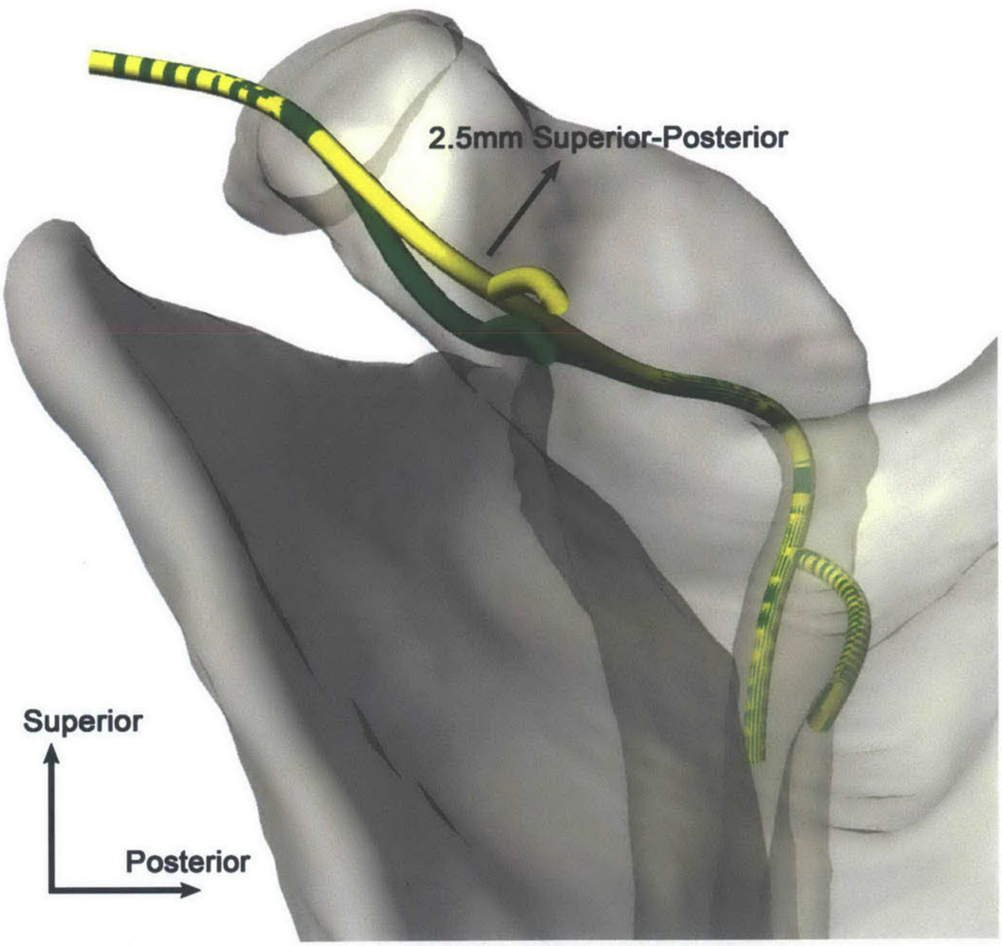

Figure 18 A medial view illustration of the anatomic SSN with an intact rotator cuff shown in green (case #1). Shown in yellow is the SSN course with a transosseous double row repair of the tendons with transection of the transverse scapular ligament (case #5).

4.6 *Discussion*

This pilot study was designed as a proof of concept to evaluate a system designed to determine the SSN anatomy during shoulder motion with simulated rotator cuff muscle forces and with simulated rotator cuff tendon tears and/or with transection of the transverse scapular ligament. In a cadaver, we established a 3D model for the dynamic SSN course in the abducted/adducted shoulder. Empirically we were able to detect medial traction about the spinoglenoid notch following the simulated massive rotator cuff tendon tear; and this effect was reversed by anatomic transosseous footprint repair. Furthermore, release of the transverse scapular ligament allowed the SSN to move superior-posterior out of the suprascapular notch, with a more direct or shorter nerve path to mitigate the medializing tendencies of a concomitant massive posterosuperior rotator cuff tendon tear.

A number of proposed mechanisms for injury to the SSN exist in the literature. Repetitive traction in overhead athletes,[10,17] microemboli from the axillary artery,[22] a stenotic suprascapular notch,[21,22] iatrogenic injury,[27] or direct pressure from a cyst or bone tumor have all been proposed.[1,9,14,24,29,30] The common pathway is generally direct pressure or stretch on the SSN. This pilot study provides proof for the concept that a retracted posterosuperior rotator cuff tendon tear puts the nerve in tension at the notches that constrain the SSN.

The link between the rotator cuff pathology and SSN dysfunction began with anatomic studies examining the surgical advancement of the superior rotator cuff during open repair. A 1992 study by Warner et al found that greater than 3cm of rotator cuff advancement places tension on the medial motor branches.[28] These findings were corroborated by a later anatomic study by Grenier et al that demonstrated measurable stretch on the motor branch with only 1cm of tendon advancement.[11]

The first cadaveric study to examine rotator cuff tendon retraction as a pathologic entity for the SSN was conducted in 2003 by Albritton et al.[2] In that static anatomic study, they demonstrated that increasing retraction of the supraspinatus led to a reduction in the angle between the SSN and the first motor branch, thereby increasing tension on the nerve.

That study established that anatomic change in nerve tracking was a potential causal link between a retracted rotator cuff tendon tear and SSN injury.

Vad et al used electrodiagnostic testing to examine the prevalence of peripheral neurologic injury in 25 patients with full-thickness rotator cuff tendon tears and gross muscle atrophy.[25] They found a 28% prevalence of nerve injury, most commonly of the axillary or suprascapular nerves. In a 2006 study, Mallon et al reported on eight patients with massive rotator cuff tendon tears retracted at least 5cm in greatest dimension.[18] All eight had SSN denervation on electromyography (EMG). Four patients consented to partial repair with good functional results. Two of the repaired patients consented to follow up EMG, which demonstrated significant reinervation potentials.

In a recent study by Coustoros et al they demonstrated that partial repair of the posterior rotator cuff tendon in patients with massive rotator cuff tendon tears leads to reversal of SSN denervation on EMG.[6] At six months post repair, all six patients had evidence of recovery by EMG potentials. It was presumed this was the result of relieving traction on the nerve by restoring its normal course through the spinoglenoid notch when the posterior rotator cuff tendon was repaired. The results of our pilot study empirically support their presumption that the SSN moves lateral, away from the spinoglenoid, restoring SSN anatomy with repair of retracted posterosuperior rotator cuff tendons.

In 2007, Lafosse et al published an arthroscopic technique for release of the SSN at the transverse scapular notch.[16] They demonstrated the effectiveness of this method in both alleviating pain and reversing EMG findings in patients with electrodiagnostically documented SSN neuropathy. Both Lafosse et al[16] and Romeo et al[23] have proposed that release of the SSN at the time of rotator cuff tendon repair is appropriate in select patients to relieve traction on the SSN, which is a direct result from tendon retraction.

Our empirical results provide a novel proof of concept model to further evaluate the previous clinical observations of clinical improvement and EMG reversal of SSN neuropathy,[6,16] which is that repair of rotator cuff tendon tears and/or release of the SSN at the transverse scapular notch reduces traction on the nerve. This anatomic pilot study is the first to devise a methodology to explore both the effect of rotator cuff tendon repair and/or transverse scapular ligament release on the SSN. As such, this study evaluated the SSN anatomy in a physiologically relevant model with applied rotator cuff muscle forces during dynamic shoulder abduction/adduction using a validated DFIS 3D modeling technique. The anatomic course of the SSN was modeled with and without a simulated rotator cuff tendon tear and repair and/or with transection of the transverse scapular ligament.

There are, however, several limitations of our study. First, as with all cadaver studies, an assumption must be made regarding physiologic muscle forces about the shoulder. We were careful to weight each muscle individually, dynamically, and in proportion to its cross sectional area according to precedent set in prior study.[20] We radiographically confirmed that the humeral head remained concentric on the glenoid during shoulder motion. Second, only one cadaver shoulder was used to quantify the motion of the SSN in a simulated massive rotator cuff tendon tear, tendon repair, and release of the transverse scapular ligament. Ultimately, our study goal to biomechanically demonstrate the concept that SSN anatomy can be evaluated with this novel DFIS technique to determine whether the course of the SSN under varying conditions such as a rotator cuff tendon tear and/or release of the transverse scapular ligament was accomplished. This pilot study provides evidence for future study regarding the influence of rotator cuff tendon tears and release of the transverse scapular ligament on SSN course alteration. The concepts of this pilot study, however, may have limited generalizability given the young age of the cadaver, lack of cuff pathology, and most common variant of SSN and suprascapular notch anatomy.

Conclusion: This pilot study demonstrated that a novel DFIS technique can evaluate dynamic SSN anatomy and that the anatomical course of the SSN may be altered by a rotator cuff tendon tear. Moreover, we believe that this model provides proof for the concept that SSN traction injury may occur in the clinical setting of a massive rotator cuff tendon tear, and has the potential to be reversed by anatomic repair and/or transverse scapular ligament release. Further study is warranted.

4.7 References

1. Abboud, J. A.; Silverberg, D.; Glaser, D. L.; Ramsey, M. L.; and Williams, G. R.: Arthroscopy effectively treats ganglion cysts of the shoulder. *Clin Orthop Relat Res,* 444: 129-33, 2006.

2. Albritton, M. J.; Graham, R. D.; Richards, R. S., 2nd; and Basamania, C. J.: An anatomic study of the effects on the suprascapular nerve due to retraction of the supraspinatus muscle after a rotator cuff tear. *J Shoulder Elbow Surg,* 12(5): 497-500, 2003.

3. Boykin, R. E.; Friedman, D. J.; Higgins, L. D.; and Warner, J. J.: Suprascapular neuropathy. *J Bone Joint Surg Am,* 92(13): 2348-64, 2010.

4. Boykin, R. E.; Friedman, D. J.; Zimmer, Z. R.; Oaklander, A. L.; Higgins, L. D.; and Warner, J. J.: Suprascapular neuropathy in a shoulder referral practice. *J Shoulder Elbow Surg,* 20(6): 983-8, 2011.

5. Chan, C. M.; Chung, C. T.; and Lan, H. H.: Scapular fracture complicating suprascapular neuropathy: the role of computed tomography with 3D reconstruction. *J Chin Med Assoc,* 72(6): 340-2, 2009.

6. Costouros, J. G.; Porramatikul, M.; Lie, D. T.; and Warner, J. J.: Reversal of suprascapular neuropathy following arthroscopic repair of massive supraspinatus and infraspinatus rotator cuff tears. *Arthroscopy,* 23(11): 1152-61, 2007.

7. Curtis, A. S.; Burbank, K. M.; Tierney, J. J.; Scheller, A. D.; and Curran, A. R.: The insertional footprint of the rotator cuff: an anatomic study. *Arthroscopy,* 22(6): 609 e1, 2006.

8. Edelson, J. G.: Bony bridges and other variations of the suprascapular notch. *J Bone Joint Surg Br,* 77(3): 505-6, 1995.

9. Fehrman, D. A.; Orwin, J. F.; and Jennings, R. M.: Suprascapular nerve entrapment by ganglion cysts: a report of six cases with arthroscopic findings and review of the literature. *Arthroscopy,* 11(6): 727-34, 1995.

10. Ferretti, A.; Cerullo, G.; and Russo, G.: Suprascapular neuropathy in volleyball players. *J Bone Joint Surg Am,* 69(2): 260-3, 1987.

11. Greiner, A.; Golser, K.; Wambacher, M.; Kralinger, F.; and Sperner, G.: The course of the suprascapular nerve in the supraspinatus fossa and its vulnerability in muscle advancement. *J Shoulder Elbow Surg,* 12(3): 256-9, 2003.

12. Gronenschild, E.: The accuracy and reproducibility of a global method to correct for geometric image distortion in the x-ray imaging chain. *Med Phys,* 24(12): 1875-88, 1997.

13. Gronenschild, E.: Correction for geometric image distortion in the x-ray imaging chain: local technique versus global technique. *Med Phys,* 26(12): 2602-16, 1999.

14. Hazrati, Y.; Miller, S.; Moore, S.; Hausman, M.; and Flatow, E.: Suprascapular nerve entrapment secondary to a lipoma. *Clin Orthop Relat Res,* 411: 124-8, 2003.

15. Iqbal, K., and Iqbal, R.: Classification of suprascapular notch according to anatomical measurements in human scapulae. *J Coll Physicians Surg Pak,* 21(3): 169-70, 2011.

16. Lafosse, L.; Tomasi, A.; Corbett, S.; Baier, G.; Willems, K.; and Gobezie, R.: Arthroscopic release of suprascapular nerve entrapment at the suprascapular notch: technique and preliminary results. *Arthroscopy,* 23(1): 34-42, 2007.

17. Lajtai, G.; Pfirrmann, C. W.; Aitzetmuller, G.; Pirkl, C.; Gerber, C.; and Jost, B.: The shoulders of professional beach volleyball players: high prevalence of infraspinatus muscle atrophy. *Am J Sports Med,* 37(7): 1375-83, 2009.

18. Mallon, W. J.; Wilson, R. J.; and Basamania, C. J.: The association of suprascapular neuropathy with massive rotator cuff tears: a preliminary report. *J Shoulder Elbow Surg,* 15(4): 395-8, 2006.

19. Massimini, D. F.; Warner, J. J.; and Li, G.: Non-invasive determination of coupled motion of the scapula and humerus--an in-vitro validation. *J Biomech,* 44(3): 408-12, 2011.

20. Mura, N.; O'Driscoll, S. W.; Zobitz, M. E.; Heers, G.; and An, K. N.: Biomechanical effect of patch graft for large rotator cuff tears: a cadaver study. *Clin Orthop Relat Res,* 415: 131-8, 2003.

21. Plancher, K. D.; Luke, T. A.; Peterson, R. K.; and Yacoubian, S. V.: Posterior shoulder pain: a dynamic study of the spinoglenoid ligament and treatment with arthroscopic release of the scapular tunnel. *Arthroscopy,* 23(9): 991-8, 2007.

22. Ringel, S. P.; Treihaft, M.; Carry, M.; Fisher, R.; and Jacobs, P.: Suprascapular neuropathy in pitchers. *Am J Sports Med,* 18(1): 80-6, 1990.

23. Romeo, A. A.; Ghodadra, N. S.; Salata, M. J.; and Provencher, M. T.: Arthroscopic suprascapular nerve decompression: indications and surgical technique. *J Shoulder Elbow Surg,* 19(2 Suppl): 118-23, 2010.

24. Semmler, A.; von Falkenhausen, M.; and Schroder, R.: Suprascapular nerve entrapment by a spinoglenoid cyst. *Neurology,* 70(11): 890, 2008.

25. Vad, V. B.; Southern, D.; Warren, R. F.; Altchek, D. W.; and Dines, D.: Prevalence of peripheral neurologic injuries in rotator cuff tears with atrophy. *J Shoulder Elbow Surg,* 12(4): 333-6, 2003.

26. Vorster, W.; Lange, C. P.; Briet, R. J.; Labuschagne, B. C.; du Toit, D. F.; Muller, C. J.; and de Beer, J. F.: The sensory branch distribution of the suprascapular nerve: an anatomic study. *J Shoulder Elbow Surg,* 17(3): 500-2, 2008.

27. Wang, J.; Singh, A.; Higgins, L.; and Warner, J.: Suprascapular neuropathy secondary to reverse shoulder arthroplasty: a case report. *J Shoulder Elbow Surg,* 19(3): e5-8, 2010.

28. Warner, J. P.; Krushell, R. J.; Masquelet, A.; and Gerber, C.: Anatomy and relationships of the suprascapular nerve: anatomical constraints to mobilization of the supraspinatus and infraspinatus muscles in the management of massive rotator-cuff tears. *J Bone Joint Surg Am,* 74(1): 36-45, 1992.

29. Westerheide, K. J.; Dopirak, R. M.; Karzel, R. P.; and Snyder, S. J.: Suprascapular nerve palsy secondary to spinoglenoid cysts: results of arthroscopic treatment. *Arthroscopy,* 22(7): 721-7, 2006.

30. Yi, J. W.; Cho, N. S.; and Rhee, Y. G.: Intraosseous ganglion of the glenoid causing suprascapular nerve entrapment syndrome: a case report. *J Shoulder Elbow Surg,* 18(3): e25-7, 2009.

Chapter 5: Summary and Future Directions

In this thesis, I accomplished five principal objectives. (1) I described and validated a non-invasive DFIS to measure dynamic shoulder joint motion; (2) I described a technique to quantify in-vivo glenohumeral joint contact patterns from the measured shoulder motion; (3) I quantified normal glenohumeral joint contact patterns in the young healthy adult; (4) I compared glenohumeral joint contact patterns determined both with and without articular cartilage data; and (5) I demonstrated that the DFIS technique can evaluate the dynamic suprascapular nerve anatomy in 6-DOF in a cadaveric model and showed that the anatomical course of the nerve may be altered by injury and subsequent to surgical intervention.

The significance of this thesis is that it presents a validated non-invasive method to measure in-vivo shoulder joint kinematics and subsequently quantify in-vivo glenohumeral joint contact patterns. As a result, this technique may be more sensitive than traditional 6-DOF glenohumeral joint kinematic measurements for the assessment of overall glenohumeral joint health both in the injured joint state and after surgical intervention. This technique will let us test the hypothesis and ask: What are normal in-vivo glenohumeral joint contact patterns, are they altered in the injured and surgically augmented state, and will these altered joint contact patterns serve to initiate and progress osteoarthritis (OA) in-vivo? Many of the premier surgical interventions for shoulder joint pathology rely on the implicit belief that glenohumeral joint contact patterns must be restored to normal in order to obtain good clinical outcomes, with a potential benefit of delaying the onset and progression of OA. However, this belief has not been tested, as prior to this thesis, there did not exist a technique to quantify in-vivo glenohumeral joint articular cartilage contact patterns. Therefore, in the future, we hope that this technique will be used to quantify the effects that injury (e.g., glenohumeral joint instability and rotator cuff disease) and surgical intervention have on the long-term ability to restore in-vivo glenohumeral joint contact patterns to normal. The results of these future studies will help to determine whether the restoration of glenohumeral joint contact patterns to normal are necessary to obtain good clinical outcomes and whether the restoration serves to delay the onset and progression of OA.